Giant Plasmene Nanosheets, Nanoribbons, and Origami

Kae Jye Si,[†,‡,▽] Debabrata Sikdar,[§,▽] Yi Chen,[†,‡] Fatima Eftekhari,[‡] Zaiquan Xu,[⊥] Yue Tang,[†,‡] Wei Xiong,[†,‡] Pengzhen Guo,[†,‡] Shuang Zhang,[∥] Yuerui Lu,[∥] Qiaoliang Bao,[#,⊥] Weiren Zhu,[§] Malin Premaratne,[§] and Wenlong Cheng[*,†,‡]

[†]Department of Chemical Engineering, Faculty of Engineering, Monash University, Clayton 3800, Victoria, Australia, [‡]The Melbourne Centre for Nanofabrication, 151 Wellington Road, Clayton 3168, Victoria, Australia, [§]Advanced Computing and Simulation Laboratory (AχL), Department of Electrical and Computer Systems Engineering, Faculty of Engineering, Monash University, Clayton 3800, Victoria, Australia, [⊥]Department of Materials Engineering, Faculty of Engineering, Monash University, Clayton 3800, Victoria, Australia, [∥]Research School of Engineering, College of Engineering and Computer Science, Australian National University, Canberra 0200, Australian Capital Territory, Australia, and [#]FUNSOM and Collaborative Innovation Center of Suzhou Nano Science and Technology, Soochow University, Suzhou 215123, P. R. China. [▽]These authors contributed equally.

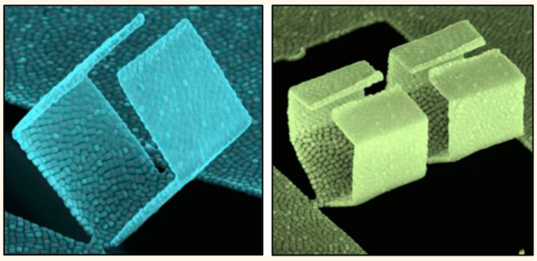

ABSTRACT We introduce *Plasmene*— in analogy to graphene—as free-standing, one-particle-thick, superlattice sheets of nanoparticles ("meta-atoms") from the "plasmonic periodic table", which has implications in many important research disciplines. Here, we report on a general bottom-up self-assembly approach to fabricate giant plasmene nanosheets (*i.e.*, plasmene with nanoscale thickness but with macroscopic lateral dimensions) as thin as ~40 nm and as wide as ~3 mm, corresponding to an aspect ratio of ~75 000. In conjunction with top−down lithography, such robust giant nanosheets could be milled into one-dimensional nanoribbons and folded into three-dimensional origami. Both experimental and theoretical studies reveal that our giant plasmene nanosheets are analogues of graphene from the plasmonic nanoparticle family, simultaneously possessing unique structural features and plasmon propagation functionalities.

KEYWORDS: self-assembly · giant · plasmene · nanosheet · nanoribbon · origami · graphene

Although the past two decades have witnessed the emergence of various superlattice materials from quantum dots,[1−3] magnetic[2,4,5] and metal[6−23] nanoparticles, and even protein,[24] their plasmonic properties did not draw much attention until recently.[11,25−27] Plasmon hybridization theory[28] predicts the resonance coupling in structurally well-defined nanoparticle assemblies including plasmonic molecules, polymers, two-dimensional (2D) and three-dimensional (3D) superlattices.[29] In particular, for free-standing plasmonic nanoparticle superlattice sheets (termed plasmene), the hybridized plasmon modes and near-field distributions can be strictly controlled in a 2D plane, which can in principle be programmed by adjusting the sizes and shapes of the constituent nanoparticles and varying the interparticle spacing (note that porous metallic sheets were previously defined as plasmene rolls;[30] however, our plasmene is built from elemental nanoparticle building blocks, a true analogue to graphene). The ability to fabricate plasmene nanosheets is of fundamental significance for understanding the large-scale 2D self-assembly, and of practical significance for engineering of flexible/stretchable plasmonic devices and circuits. Despite a few recent examples of free-standing plasmonic nanoparticle superlattices,[5,11,16,27,31] none of them can meet the requirement of giant plasmene nanosheets, let alone further manufacturing into 1D or 3D plasmonic structures. Using bimetallic Au@Ag nanocubes (NCs) as model building blocks, we demonstrate a general self-assembly approach to fabricate giant plasmene nanosheets, which can be further shaped into nanoribbons and origamis in conjunction with top−down focused ion beam (FIB) lithography.

RESULTS AND DISCUSSION

We begin with synthesis of monodisperse Au@Ag NCs by following the recently reported protocols[32] with some minor modifications. In brief, gold nanospheres with diameter of ~11 nm were synthesized and

* Address correspondence to wenlong.cheng@monash.edu.

Received for review August 17, 2014 and accepted September 29, 2014.

10.1021/nn504615a

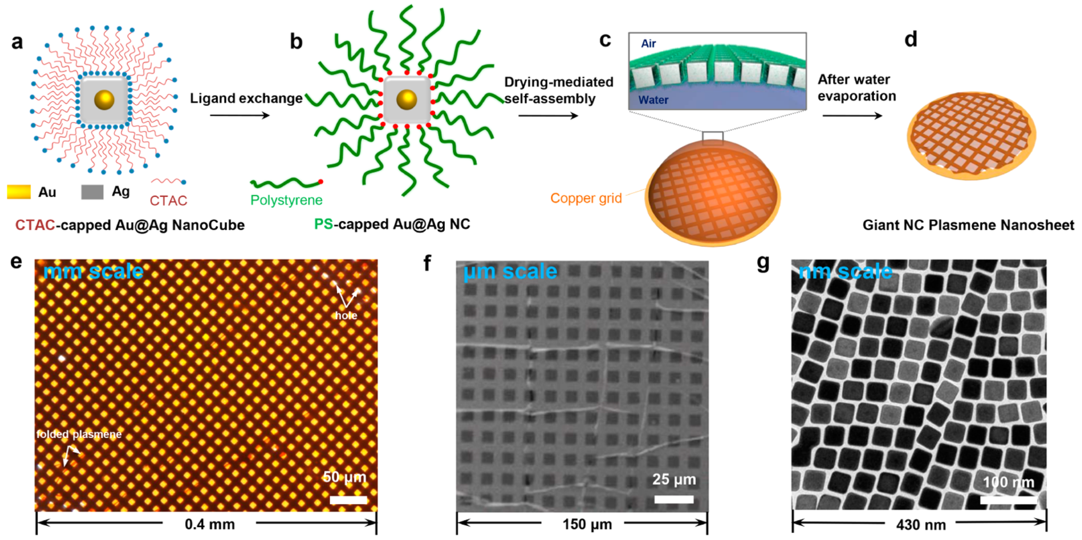

Figure 1. Fabrication of giant NC-plasmene nanosheets. (a−d) Schematic of fabrication process of NC-plasmene nanosheets by ligand exchange in conjunction with drying-mediated self-assembly. Characterization of giant NC-plasmene nanosheets at the (e) macro-, (f) micro-, and (g) nanoscale by optical microscope, SEM, and TEM, respectively.

used as cores, and a uniform coating layer of silver was deposited on them. The average edge lengths of the as-synthesized NCs can be tuned from $\sim$21 to $\sim$33 nm. Such NCs exhibit well-pronounced dipolar, quadrupolar and octopolar localized surface plasmon resonance (LSPR) bands[33] (see Supporting Information Figures S1 and S2). Notably, the pristine NCs were stabilized by hexadecyltrimethylammonium chloride (CTAC), a weak-binding ligand, which nevertheless provides insufficient protection from random nanoparticle aggregation. Therefore, a two-step ligand exchange procedure[27,31] was applied to replace CTAC by a much stronger binding ligand, thiolated-polystyrene (PS) (M_n = 50 000 g mol^{-1}) (Figure 1).

To grow giant plasmene nanosheets, a droplet of concentrated chloroform solution of PS-capped NCs was spread onto a sessile water drop on a holey copper grid (2000 mesh with hole-size of 7 μm × 7 μm, Figure 1c). Rapid chloroform evaporation confined the self-assembly of PS-capped NCs at the air/water interface forming monolayered nanosheet patches. Subsequent slow water evaporation reduced the interface area by about 50% from a hemisphere-like surface to a pancake-like surface. This process gradually fused the patchy nanosheets into giant nanosheets covering the entire holey substrate. Such-formed plasmene sheets could have a lateral dimension of $\sim$3 mm and a thickness of $\sim$40 nm, corresponding to an aspect ratio of $\sim$75 000.

At the macroscopic scale, the plasmene sheets were readily observable under an optical microscope with distinct colors (Figure 1e); at the microsocopic scale, the plasmene sheets were monolayered yet flexible (Figure 1f); at the nanoscopic scale, NCs were in ordered packing (Figure 1g). The quality of giant plasmene nanosheets critically depended on the length of the polymer ligands but was almost independent of the type of substrates. Strikingly, our giant plasmene nanosheets could be even shaped into desired shapes and patterned into regular arrays. Atomic force microscope (AFM) line scanning further proved that our plasmene nanosheets were single-particle-thick, with an average thickness of 40 ± 2 nm. Despite being extremely thin, the sheets were mechanically strong, with a typical Young's modulus of $\sim$1 GPa, as derived from the AFM nanoindentation (see Supporting Information Figure S4). The robustness of our plasmene sheets allows one to use them as mechanical membrane resonators with fundamental resonance frequencies ranging from 40 to 220 kHz. The measured quality factors of such resonators exceeded 100 in air, which is about 1 order of magnitude larger than the quality factors of alkyl-nanoparticle superlattice sheets[34] (see Supporting Information Figure S5).

The NC-based plasmene sheets exhibit strong plasmonic resonance peaks in the extinction spectra. High-precision numerical simulations are then carried out to identify the dominant plasmon modes corresponding to the extinction peaks. The structural parameters of the plasmene sheet were extracted from the representative TEM images (Figure 2a) and used in numerical simulations based on CST Microwave Studio Suite. Figure 2b depicts the near-field distribution pattern calculated along the *z*-plane passing through the center of the NC plasmene sheet. Strong electromagnetic fields are seen to be highly localized in the internanoparticle gaps. A direct correlation can be observed where narrower gaps led to stronger filed confinement. This localized near-field gets enhanced due to the plasmonic coupling between the nanoparticles, and the plasmonic gap resonance arises from the standing wave mode sustained by the capacitive

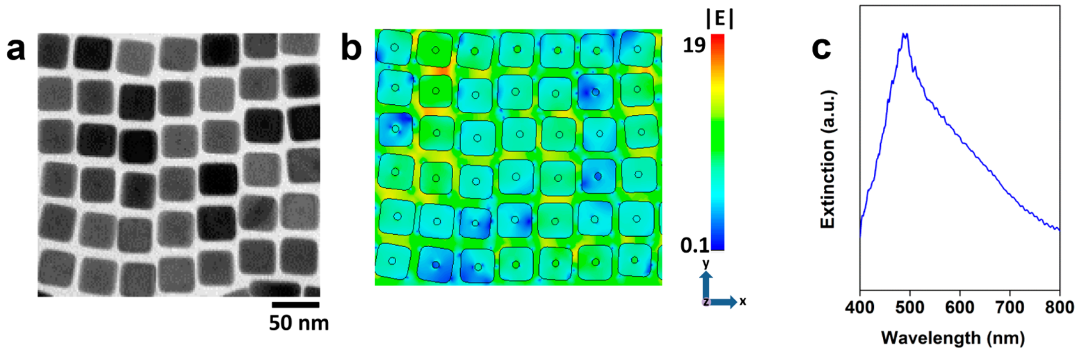

Figure 2. Plasmonic properties of giant NC-plasmene nanosheet. (a) Representative TEM image for NC plasmene sheet used to simulate (b) near-field distributions when excited with light having a free space wavelength of 490 nm. (c) Experimental extinction spectrum of the NC plasmene sheet.

coupling between the adjacent nanoparticles.[35] The observed peak in the extinction spectrum (Figure 2c) corresponds to the resonance of the gap plasmons confined to 2D planes.

In addition to gap plasmon modes, our plasmene sheets could also support plasmon propagating on their top surfaces. We extracted the exact size distribution and interparticle spacing from the TEM image in Figure 2a, and used the ensemble as a unit cell to form a 2D giant plasmene sheet. Simulation shows that when light from an excitation port falls over a small area in the center of the sheet, plasmon excitation can propagate across the entire sheet following a cylindrical wave pattern (see Supporting Information Figure S6, Supporting Information Movies 1 and 2). Numerically calculated field-amplitude decay time of the plasmon excitations provides additional evidence of decaying surface plasmon resonances with 1/e–amplitude decay time of ~11 fs (see Supporting Information Figure S7), which is significantly longer than the decay time of localized surface plasmons of isolated metal nanoparticles[36] (~6 fs) and is comparable to the reported value for a nanocrystal superlattice.[35]

To further verify the propagating nature of the excited plasmons, we transferred the plasmene nanosheets onto side-polished D-shape optical fiber to form a hybrid fiber-to-plasmene waveguide coupler (see Supporting Information Figure S8). By investigating the polarization of the output light from this coupler, we were able to determine the nature of the propagating surface wave. Unlike graphene, which supports transverse electric (TE) propagating waves,[37–39] our plasmene sheets selectively support transverse magnetic (TM) propagating waves, with electric field perpendicular to the sheet's surface. This is because the fiber-to-plasmene coupler has a metal–dielectric interface where TE surface wave is forbidden and only the vertically polarized plasmons can propagate through the plasmene sheet (see Supporting Information Figure S9). We obtained a polarization extinction ratio exceeding 10 dB, which is comparable to that of the solid metal film-based polarizers.[40]

Analogous to graphene, our plasmene sheets could be milled into free-standing nanoribbons without any fracture by FIB lithography (Figure 3a–e). We fabricated 3-, 4-, 6-, 8-, and 11-particle-wide NC plasmene nanoribbons, corresponding to widths of 113 ± 10, 206 ± 8, 305 ± 8, 405 ± 8, and 502 ± 11 nm, respectively. All the nanoribbons had smooth top surfaces and the NC particles remained ordered after FIB milling. Both theoretical and experimental results (Figure 3f,g) indicated evident width-dependent properties, analogous to plasmonic properties of graphene nanoribbons.[41] From the simulated extinction spectra of perfectly ordered NCs arranged in shape of ribbons (Figure 3f), we can identify two main trends similar to those reported for graphene nanoribbons when the ribbon width increases: (1) the main characteristic resonance peaks i, ii, iii (corresponding to edge-coupled, corner-coupled and edge-corner-coupled modes, respectively; see Supporting Information Figure S11) exhibited an overall trend of red-shift with increasing ribbon width but at different dispersion rates (Figure 3f). Peak iii disperses a faster rate than peaks i and ii and, hence, exhibits the most prominent red-shift, and (2) the peak iii intensity of the extinction spectra was observed to grow linearly with increasing nanoribbon width (Figure 3g). Note that each extinction spectrum also exhibits a few more low energy peaks/shoulders. The origin of all these spectral features are thoroughly investigated using electric field-lines pattern (see Supporting Information Section II-2 and Figure S12). This helps one to identify the modes based on symmetric/antisymmetric types of coupling between different linear chains of NCs in a plasmene nanoribbon across its width, and the way these modes evolve for wider nanoribbons.

For the experimental spectra, the size dispersions of the constituent nanoparticles and interparticle spacing dispersions resulted in the merging of the weak peaks (peaks i and ii) with the strong peak iii. This can be appreciated from the fact that due to minor disordering present in the fabricated nanoribbons, the edge-coupled mode (peak i) and corner-coupled mode (peak ii)

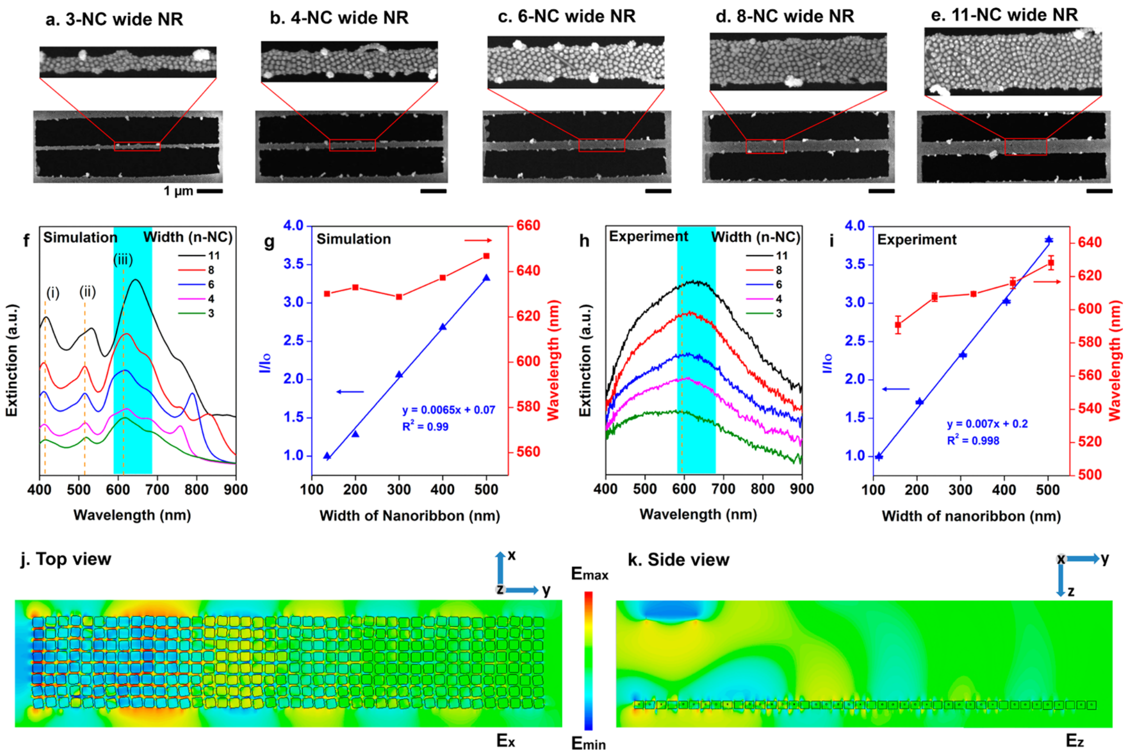

Figure 3. Characterization of plasmene nanoribbons (NRs) with different widths. (a–e) SEM characterization of plasmene nanoribbons with width of (a) ∼3, (b) 4, (c) 6, (d) 8, and (e) 11 NCs. (f) Simulated extinction spectra of the nanoribbons from (a–e) and (g) trends of peak (iii) observed in (f) with increasing nanoribbon width. Simulations are based on approximations that all NCs are identical and uniformly spaced. (h) Experimental extinction spectra of the nanoribbons from (a–e) and (i) trends of the dominant peak observed in (h) with increasing nanoribbon width. Highlighted regions indicate the dominant peak considered to investigate the effect of nanoribbon width on its optical response. (j) Top view and (k) side view of electric field distribution along the nanoribbon length (8-NC wide with length of ∼1.83 μm) showing the propagation of surface plasmons in form of waveguide mode and edge plasmon mode, when excited with light having a free space wavelength of 490 nm. The simulation is based on exact modeling of NC nanoribbon according to the representative TEM images of NC plasmene sheet shown in Figure 2a.

essentially merge to the edge-corner coupled mode (peak iii), giving rise to a wide spectrum. Moreover, due to the deviation from a perfectly ordered array as considered in simulation, the intensities of the weak low energy modes are more likely to get further reduced, and hence, they do not appear prominently in the experimental spectrum. All these eventually give rise to a broadband extinction spectrum with just one dominant peak, which is recorded experimentally. However, it is noteworthy that despite these imperfections, the trends in the peak developments (Figure 3i) are consistent with those predicted by simulations (Figure 3g), especially for the dominant peak (peak iii).

The width-dependent nanoribbon plasmonic properties can be theoretically interpreted by invoking the well-known plasmon hybridization theory.[28] The extinction resonance peak depends significantly on the strength of the bonding plasmons between NCs. The plasmon hybridization theory predicts that the resonant energy of the bonding plasmons is lower than that of discrete plasmons, leading to a spectral red shift. With increase in nanoribbon width, more number of bonding plasmons interact with each other, therefore, leading to spectral red-shift of the extinction peak.

To estimate the plasmon propagation length in a nanoribbon, we modeled a 1D NC-plasmene nanoribbon using a unit cell based on the representative TEM image (Figure 2a) by repeating the unit cell unidirectionally. The excitation port impinges light over a small area on one end of the nanoribbon, creating plasmons propagating along the length of the nanoribbon. Simulations predicted a 1/e–amplitude decay propagating length of ∼340 nm when excited with light at the gap-mode-resonance wavelength of 490 nm. This propagation length can be further increased by impinging light with shorter wavelength as losses in silver monotonously decreases with shorter wavelength. Similar to graphene nanoribbons,[42] waveguide mode and edge mode surface plasmon propagation can be observed for our plasmene nanoribbons, as seen in top view (Figure 3j, see Supporting Information Movie 3) and side view (Figure 3k, see Supporting Information Movie 4).

Remarkably, our unique plasmene nanosheets could be folded into various geometrically well-defined 3D origamis by programmed FIB-milling. The "gentle" FIB milling can partially etch the sheets, likely by removing the surface-binding polystyrene ligands and induce

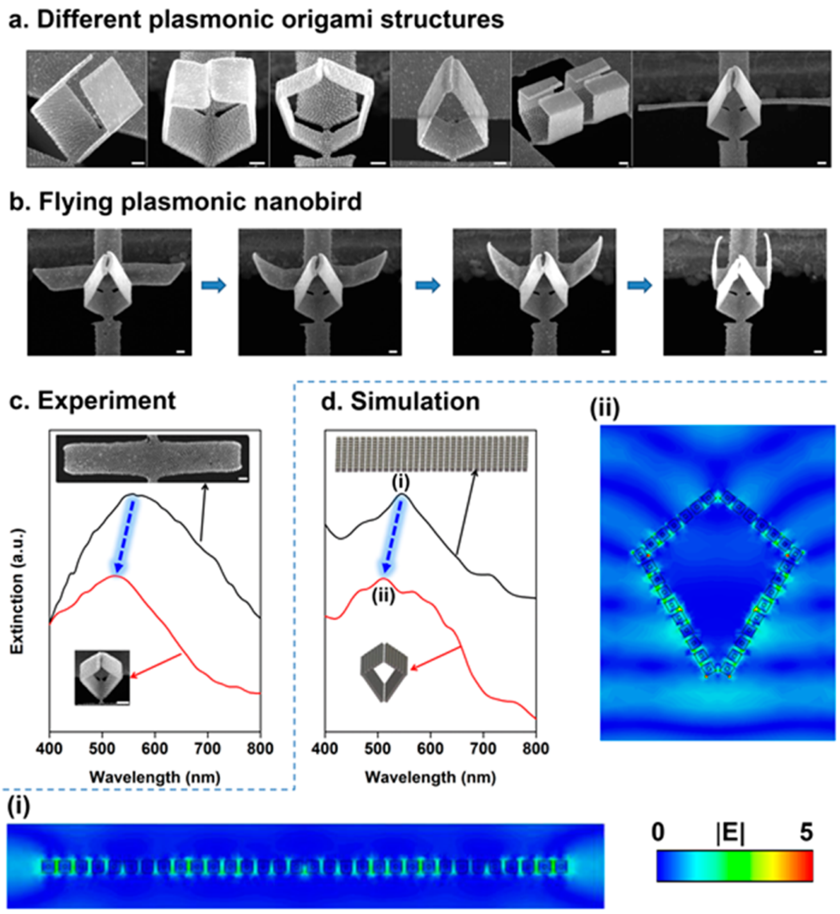

Figure 4. Plasmene origami. (a) SEM images showing the different origami structures: cube, pentagon, hexagon, diamond, hearts, and plane. (b) A series of SEM images depicting the flapping motion of a bird's wings. (c) Experimental and (d) simulation spectra for unfolded sheet and folded 3D origami structure. Insets in (c) and (d) show SEM images and simulation models of the corresponding structures, respectively. Normalized near-field distribution patterns along the cross sections of the simulation models for the peaks (i) and (ii), shown in the simulation spectra. Scale bar is 200 nm for all SEM images.

local heating,[43] which resulted in local stress buildup and folding of plasmene sheets at certain angles depending on the milling depth (see Supporting Information Figure S13). By programming the FIB-milling parameters including locations, beam current and dwelling time (see Supporting Information Section III-2), we could obtain well-defined origami structures such as cube, hexagon, pentagon, heart, air plane (Figure 4a), and even a "flying bird" (Figure 4b, see Supporting Information Movie 5). The folding angles of the bird wings can be well-controlled by programming the milling depth.

Using the 3D origami structure (shown in the inset of Figure 4c) as an example, we illustrate how folding affects plasmonic resonance properties. We found that plasmonic peak shifted to blue with narrowing bandwidth when unfolded nanoribbon was crafted into a 3D origami. Consistent with experimental observations (Figure 4c), the numerical simulations also predicted blue shift with folding (Figure 4d). The blue shift may be attributed to reduction in plasmonic interactions owing to incoherent interparticle coupling between the nanocubes of the origami structure. This may be attributed to the fact that for an origami structure, incident light reaches the nanoparticles (at different heights) of the side planes of the 3D origami at different phases. The near-field distribution patterns obtained along the cross section of an unfolded nanoribbon (Figure 4d (i)) and folded 3D origami (Figure 4d (ii)) also testify the change in near-field coupling between adjacent nanocubes of the ribbon upon folding.

The effect of folding of a plasmene nanoribbon on its optical response is further investigated by numerically evaluating the extinction spectra of single-folded ribbons with different folding angles (see Supporting Information Section III-3). The trend of spectral evolution of plasmon resonance peaks with increasing folding angles is shown in Supporting Information Figure S20. A comparative analysis of the normalized near-field distribution patterns (see Supporting Information Figures S21 and S22) allow one to appreciate folding-induced spectral evolution of the dominant resonance peak. On the basis of these findings, we analyzed and explained the blue shift in the evolution of optical spectrum for a multifolded 3D origami shown in

Figure 4d (see Supporting Information Section III-3 and Figure S23). Although, some minor differences were noted between the simulated and experimental spectra, these can be attributed to the fact that all the NCs are considered to be identical and uniformly spaced in the simulations (see Supporting Information Figure S23).

CONCLUSION

In summary, we have demonstrated a robust general approach to fabricate giant plasmene nanosheets which exhibit analogous properties to graphene as well as some unique features. Similar to graphene, our plasmene is mechanically robust, and can be used as a mechanical resonator; it can also support propagating plasmons and be shaped into 1D nanoribbons with width-dependent plasmonic properties. Despite their structural imperfection, our first version of plasmene sheets have exhibited a number of unique features: (1) plasmene could be, in principle, customized arbitrarily using various “meta-atoms” elements from the artificial metamaterial periodic table;[29] (2) the hybrid organic/inorganic composition of our plasmene sheets enabled the fabrication of 3D origami structures. Given the generality of the concepts and methodologies established here, we believe that plasmene materials will lead to a wide range of scientific and technological applications, like flexible and stretchable plasmonics, foldable plasmonic devices, plasmonic waveguiding, switching and sensing, *etc*.

METHODS

Materials. Gold(III) chloride trihydrate ($HAuCl_4 \cdot 3H_2O$, ≥99.9%), hexadecyltrimethylammonium bromide (CTAB), cetyltrimethylammonium chloride solution (CTAC, 25 wt % in H_2O), silver nitrate ($AgNO_3$), sodium borohydride ($NaBH_4$) and L-ascorbic acid were purchased from Sigma-Aldrich. Tetrahydrofuran (THF) and chloroform were obtained from Merck KGaA. Thiol-functionalized polystyrene (M_n = 50 000 g/mol, M_w/M_n = 1.06) was purchased from Polymer Source, Inc. All chemicals were used as-received unless otherwise indicated. Demineralized water was used in all aqueous solutions, which were further purified with a Milli-Q system (Millipore). All glassware used in the following procedures was cleaned in a bath of freshly prepared *aqua regia* and rinsed thoroughly in H_2O prior to use.

Gilder extra fine bar grids (2000 mesh with 7 × 7 μm^2 square holes) were purchased from Ted Pella. Holey silicon nitride support films (2-μm-diameter hole, 4 μm pitch) were purchased from SPI supplies.

Synthesis of Polystyrene-Capped Au@Ag NCs. The synthesis of high-quality CTAC-capped Au@Ag NCs was achieved by adopting the slightly modified recently developed approaches[32] (see Supporting Information Section I-1). Replacement of CTAC with thiolated PS was achieved using a two-step ligand-exchange procedure.[27,31] The as-prepared CTAC-stabilized Au@Ag NCs (5 mL) were typically spun down and concentrated into 0.1 mL, followed by dropwise addition of the above concentrated Au@Ag NCs to an excess thiol-functionalized polystyrene solution (dissolved in THF, 2 mg mL^{-1}) under vigorous stirring. After aging overnight at room temperature, the supernatant was discarded and the samples were purified by repeated centrifugation–precipitation cycles and redispersed in chloroform as a stock solution.

Fabrication of Giant Plasmene Nanosheet. One drop of chloroform solution of PS-capped Au@Ag NCs (~27 nM) was typically spread onto the surface of convex-shape water droplet on a holey copper or silicon nitride grid. After quick chloroform evaporation, silver-colored reflective solid films formed on the water subphase. Subsequently, water slowly evaporated, leading to the formation of the giant plasmene sheets that covered almost the entire grid.

Fabrication of Nanoribbons and Origami. Plasmene sheet on a holey copper grid (7 μm × 7 μm) was bonded to ITO glass on an aluminum sample holder with conductive copper tape to eliminate any charging effect. FEI Helios Nanolab 600 FIB machine was used to generate gallium ions with an accelerating voltage of 30 kV. An ion beam current of 28 pA and a dwell time of 100 μs/100 ns were used in the experiments. The detailed patterning design and dimensions are given in the Supporting Information Section II and III.

Characterization. Electron imaging was carried out using Philips CM20 TEM or FEI Tecnai G2 T20 TEM operating at an accelerating voltage of 200 kV, or Hitachi H-7500 field emission TEM operating at 80 kV.

The optical extinction spectra of the bulk solution samples were measured using Agilent 8453 UV–vis spectrophotometer and the spectra of plasmene nanosheets, nanoribbons and origamis were obtained using J&M MSP210 microscope spectrometry system. Optical micrographs of the plasmene sheets were taken by Nikon industrial bright-field microscope (ECLIPSE LV 100D) under transmission and reflectance modes.

Mechanical properties were measured by adopting the previously reported approach.[16] Force–displacement curves and topographical structures were obtained with a Veeco Dimension Icon AFM in tapping mode using Bruker silicon probes (MPP-11120-10). The spring constant of the cantilever was 40 N m^{-1}. The typical tip speed for the nanoindentation was 500 nm s^{-1}. The AFM data was characterized using Gwyddion software.

Resonance properties were collected by mounting a piezoelectric transducer (PZT) plate driven by an electrical function generator on the backside of the membrane chip. The vibration displacement amplitude of the membrane resonator was measured by PolyTec interferometer with phase locked loop, which has a picometer resolution in vibration amplitude. During standing wave vibration amplitude 2D mapping, the driving frequency was fixed at the resonance mode and the interferometer laser gun was controlled by a stage controller for lateral movement with sub-0.5 μm lateral resolution.

Numerical Simulations. The numerical simulations of plasmene nanoribbon and origami structures were performed using CST Microwave Studio Suite. The frequency–domain FEM solver was deployed to obtain the extinction spectra of these nanostructures. Perfectly matched layer (PML) was used at the simulation domain boundaries, making the incident waves pass the boundaries with minimal reflections. Some extra space was also added in the models around the target nanostructure within the open boundaries to enable far-field calculations. Tetrahedral mesh, which is more accurate at metallic material interfaces, was used in the frequency–domain simulations with automatic mesh refinement to study the optical response over the wavelength window of interest. An adaptive hexahedral meshing was considered for time–domain simulations. Steady-state accuracy limit of −60 dB was considered in all the time–domain studies reported here.

Conflict of Interest: The authors declare no competing financial interest.

Supporting Information Available: Detailed description of the experimental procedures and theoretical simulations employed for this work; movies of plamene sheets, nanoribbons, and origami structures (.zip). This material is available free of charge *via* the Internet at http://pubs.acs.org.

Acknowledgment. M.P., W.Z., and W.L.C. acknowledge Discovery Grants DP110100713, DP140100883, DP120100170, and DP140100052. This work was performed in part at the Melbourne Centre for Nanofabrication (MCN) in the Victorian Node of the Australian National Fabrication Facility (ANFF). We thank Ivan D. Rukhlenko for suggestions in modeling and Fatemeh Eftekhari for the technical support in focused ion beam lithography. The authors also gratefully acknowledge the use of facilities at Monash Micro Imaging Centre. The work of D.S. is supported by the DSDBI of the Victorian Government, through its Victoria India Doctoral Scholarship Program (managed by the Australia India Institute). Q.B. acknowledges the support from 863 Program (2013AA031903), the NSFC Grants (51222208, 51290273), ARC DECRA (DE120101569), DP (DP140101501).

Note Added after ASAP Publication: This paper published ASAP on October 2, 2014. An important author was added and the revised version was reposted on November 5, 2014.

REFERENCES AND NOTES

1. Tang, Z.; Zhang, Z.; Wang, Y.; Glotzer, S. C.; Kotov, N. A. Self-Assembly of CdTe Nanocrystals into Free-Floating Sheets. *Science* **2006**, *314*, 274–278.
2. Redl, F. X.; Cho, K. S.; Murray, C. B.; O'Brien, S. Three-Dimensional Binary Superlattices of Magnetic Nanocrystals and Semiconductor Quantum Dots. *Nature* **2003**, *423*, 968–971.
3. Kotov, N. A.; Meldrum, F. C.; Wu, C.; Fendler, J. H. Monoparticulate Layer and Langmuir-Blodgett-Type Multiparticulate Layers of Size-Quantized Cadmium Sulfide Clusters: A Colloid-Chemical Approach to Superlattice Construction. *J. Phys. Chem.* **1994**, *98*, 2735–2738.
4. Talapin, D. V.; Shevchenko, E. V.; Bodnarchuk, M. I.; Ye, X.; Chen, J.; Murray, C. B. Quasicrystalline Order in Self-Assembled Binary Nanoparticle Superlattices. *Nature* **2009**, *461*, 964–967.
5. Dong, A. G.; Chen, J.; Vora, P. M.; Kikkawa, J. M.; Murray, C. B. Binary Nanocrystal Superlattice Membranes Self-Assembled at the Liquid-Air Interface. *Nature* **2010**, *466*, 474–477.
6. Freeman, R. G.; Grabar, K. C.; Allison, K. J.; Bright, R. M.; Davis, J. A.; Guthrie, A. P.; Hommer, M. B.; Jackson, M. A.; Smith, P. C.; Walter, D. G.; *et al.* Self-Assembled Metal Colloid Monolayers: An Approach to SERS Substrates. *Science* **1995**, *267*, 1629–1632.
7. Whetten, R. L.; Khoury, J. T.; Alvarez, M. M.; Murthy, S.; Vezmar, I.; Wang, Z. L.; Stephens, P. W.; Cleveland, C. L.; Luedtke, W. D.; Landman, U. Nanocrystal Gold Molecules. *Adv. Mater.* **1996**, *8*, 428–433.
8. Collier, C. P.; Saykally, R. J.; Shiang, J. J.; Henrichs, S. E.; Heath, J. R. Reversible Tuning of Silver Quantum Dot Monolayers through the Metal-Insulator Transition. *Science* **1997**, *277*, 1978–1981.
9. Kiely, C. J.; Fink, J.; Brust, M.; Bethell, D.; Schiffrin, D. J. Spontaneous Ordering of Bimodal Ensembles of Nanoscopic Gold Clusters. *Nature* **1998**, *396*, 444–446.
10. Courty, A.; Mermet, A.; Albouy, P. A.; Duval, E.; Pileni, M. P. Vibrational Coherence of Self-Organized Silver Nanocrystals in f.c.c. Supra-Crystals. *Nat. Mater.* **2005**, *4*, 395–398.
11. Tao, A.; Sinsermsuksakul, P.; Yang, P. Tunable Plasmonic Lattices of Silver Nanocrystals. *Nat. Nanotechnol.* **2007**, *2*, 435–440.
12. Henzie, J.; Grünwald, M.; Widmer-Cooper, A.; Geissler, P. L.; Yang, P. Self-Assembly of Uniform Polyhedral Silver Nanocrystals into Densest Packings and Exotic Superlattices. *Nat. Mater.* **2012**, *11*, 131–137.
13. Cheng, W. L.; Hartman, M. R.; Smilgies, D. M.; Long, R.; Campolongo, M. J.; Li, R.; Sekar, K.; Hui, C. Y.; Luo, D. Probing in Real Time the Soft Crystallization of DNA-Capped Nanoparticles. *Angew. Chem., Int. Ed.* **2010**, *49*, 380–384.
14. Park, S. Y.; Lytton-Jean, A. K. R.; Lee, B.; Weigand, S.; Schatz, G. C.; Mirkin, C. A. DNA-Programmable Nanoparticle Crystallization. *Nature* **2008**, *451*, 553–556.
15. Nykypanchuk, D.; Maye, M. M.; van der Lelie, D.; Gang, O. DNA-Guided Crystallization of Colloidal Nanoparticles. *Nature* **2008**, *451*, 549–552.
16. Cheng, W. L.; Campolongo, M. J.; Cha, J. J.; Tan, S. J.; Umbach, C. C.; Muller, D. A.; Luo, D. Free-Standing Nanoparticle Superlattice Sheets Controlled by DNA. *Nat. Mater.* **2009**, *8*, 519–525.
17. Mueggenburg, K. E.; Lin, X. M.; Goldsmith, R. H.; Jaeger, H. M. Elastic Membranes of Close-Packed Nanoparticle Arrays. *Nat. Mater.* **2007**, *6*, 656–660.
18. Korgel, B. A. Nanocrystal Superlattices Assembly at Liquid Interfaces. *Nat. Mater.* **2010**, *9*, 701–703.
19. Auyeung, E.; Cutler, J. I.; Macfarlane, R. J.; Jones, M. R.; Wu, J.; Liu, G.; Zhang, K.; Osberg, K. D.; Mirkin, C. A. Synthetically Programmable Nanoparticle Superlattices Using a Hollow Three-Dimensional Spacer Approach. *Nat. Nanotechnol.* **2012**, *7*, 24–28.
20. Bigioni, T. P.; Lin, X. M.; Nguyen, T. T.; Corwin, E. I.; Witten, T. A.; Jaeger, H. M. Kinetically Driven Self Assembly of Highly Ordered Nanoparticle Monolayers. *Nat. Mater.* **2006**, *5*, 265–270.
21. Gong, J.; Li, G.; Tang, Z. Self-Assembly of Noble Metal Nanocrystals: Fabrication, Optical Property, and Application. *Nano Today* **2012**, *7*, 564–585.
22. Zhu, Z.; Meng, H.; Liu, W.; Liu, X.; Gong, J.; Qiu, X.; Jiang, L.; Wang, D.; Tang, Z. Superstructures and SERS Properties of Gold Nanocrystals with Different Shapes. *Angew. Chem., Int. Ed.* **2011**, *50*, 1593–1596.
23. Ming, T.; Kou, X.; Chen, H.; Wang, T.; Tam, H. L.; Cheah, K. W.; Chen, J. Y.; Wang, J. Ordered Gold Nanostructure Assemblies Formed By Droplet Evaporation. *Angew. Chem., Int. Ed.* **2008**, *47*, 9685–9690.
24. Kostiainen, M. A.; Hiekkataipale, P.; Laiho, A.; Lemieux, V.; Seitsonen, J.; Ruokolainen, J.; Ceci, P. Electrostatic Assembly of Binary Nanoparticle Superlattices Using Protein Cages. *Nat. Nanotechnol.* **2013**, *8*, 52–56.
25. Ye, X.; Chen, J.; Diroll, B. T.; Murray, C. B. Tunable Plasmonic Coupling in Self-Assembled Binary Nanocrystal Superlattices Studied by Correlated Optical Microspectrophotometry and Electron Microscopy. *Nano Lett.* **2013**, *13*, 1291–1297.
26. Chen, C. F.; Tzeng, S. D.; Chen, H. Y.; Lin, K. J.; Gwo, S. Tunable Plasmonic Response from Alkanethiolate-Stabilized Gold Nanoparticle Superlattices: Evidence of Near-Field Coupling. *J. Am. Chem. Soc.* **2007**, *130*, 824–826.
27. Ng, K. C.; Udagedara, I. B.; Rukhlenko, I. D.; Chen, Y.; Tang, Y.; Premaratne, M.; Cheng, W. L. Free-Standing Plasmonic-Nanorod Superlattice Sheets. *ACS Nano* **2011**, *6*, 925–934.
28. Prodan, E.; Radloff, C.; Halas, N. J.; Nordlander, P. A Hybridization Model for the Plasmon Response of Complex Nanostructures. *Science* **2003**, *302*, 419–422.
29. Tan, S. J.; Campolongo, M. J.; Luo, D.; Cheng, W. L. Building Plasmonic Nanostructures with DNA. *Nat. Nanotechnol.* **2011**, *6*, 268–276.
30. Huang, F. M.; Sinha, J. K.; Gibbons, N.; Bartlett, P. N.; Baumberg, J. J. Direct Assembly of Three-Dimensional Mesh Plasmonic Rolls. *Appl. Phys. Lett.* **2012**, *100*, 193107.
31. Chen, Y.; Fu, J.; Ng, K. C.; Tang, Y.; Cheng, W. L. Free-Standing Polymer-Nanoparticle Superlattice Sheets Self-Assembled at the Air Liquid Interface. *Cryst. Growth Des.* **2011**, *11*, 4742–4746.
32. Ma, Y.; Li, W.; Cho, E. C.; Li, Z.; Yu, T.; Zeng, J.; Xie, Z.; Xia, Y. Au@Ag Core−Shell Nanocubes with Finely Tuned and Well-Controlled Sizes, Shell Thicknesses, and Optical Properties. *ACS Nano* **2010**, *4*, 6725–6734.
33. Gong, J.; Zhou, F.; Li, Z.; Tang, Z. Synthesis of Au@Ag Core−Shell Nanocubes Containing Varying Shaped Cores and Their Localized Surface Plasmon Resonances. *Langmuir* **2012**, *28*, 8959–8964.
34. Kanjanaboos, P.; Lin, X. M.; Sader, J. E.; Rupich, S. M.; Jaeger, H. M.; Guest, J. R. Self-Assembled Nanoparticle Drumhead Resonators. *Nano Lett.* **2013**, *13*, 2158–2162.
35. Tao, A. R.; Ceperley, D. P.; Sinsermsuksakul, P.; Neureuther, A. R.; Yang, P. Self-Organized Silver Nanoparticles for Three-Dimensional Plasmonic Crystals. *Nano Lett.* **2008**, *8*, 4033–4038.

36. Lamprecht, B.; Krenn, J. R.; Leitner, A.; Aussenegg, F. R. Resonant and Off-Resonant Light-Driven Plasmons in Metal Nanoparticles Studied by Femtosecond-Resolution Third-Harmonic Generation. *Phys. Rev. Lett.* **1999**, *83*, 4421–4424.
37. Bao, Q.; Zhang, H.; Wang, B.; Ni, Z.; Lim, C. H. Y. X.; Wang, Y.; Tang, D. Y.; Loh, K. P. Broadband Graphene Polarizer. *Nat. Photonics* **2011**, *5*, 411–415.
38. Jablan, M.; Buljan, H.; Soljačić, M. Plasmonics in Graphene at Infrared Frequencies. *Phys. Rev. B* **2009**, *80*, 245435.
39. Mikhailov, S. A.; Ziegler, K. New Electromagnetic Mode in Graphene. *Phys. Rev. Lett.* **2007**, *99*, 016803.
40. Eickhoff, W. In-Line Fibre-Optic Polariser. *Electron. Lett.* **1980**, *16*, 762–764.
41. Yan, H.; Low, T.; Zhu, W.; Wu, Y.; Freitag, M.; Li, X.; Guinea, F.; Avouris, P.; Xia, F. Damping Pathways of Mid-Infrared Plasmons in Graphene Nanostructures. *Nat. Photonics* **2013**, *7*, 394–399.
42. Wang, J.; Lu, W. B.; Li, X. B.; Ni, Z. H.; Qiu, T. Graphene Plasmon Guided Along a Nanoribbon Coupled with a Nanoring. *J. Phys. D: Appl. Phys.* **2014**, *47*, 135106.
43. Lee, C. C.; Proust, G.; Alici, G.; Spinks, G. M.; Cairney, J. M. Three-Dimensional Nanofabrication of Polystyrene by Focused Ion Beam. *J. Microsc.* **2012**, *248*, 129–139.

SUPPORTING INFORMATION

Giant Plasmene Nanosheets, Nanoribbons and Origami

Kae Jye Si,[1,2‡] *Debabrata Sikdar,*[3‡] *Yi Chen,*[1,2] *Zaiquan Xu,*[4] *Yue Tang,*[1,2] *Wei Xiong,*[1,2] *Pengzhen Guo,*[1,2] *Shuang Zhang,*[5] *Yuerui Lu,*[5] *Qiaoliang Bao,*[4,6] *Weiren Zhu,*[3] *Malin Premaratne,*[3] *and Wenlong Cheng* [1,2]*

[1]Department of Chemical Engineering, Faculty of Engineering, Monash University, Clayton 3800, Victoria, Australia

[2]The Melbourne Centre for Nanofabrication, 151 Wellington Road, Clayton 3168, Victoria, Australia

[3]Advanced Computing and Simulation Laboratory (AχL), Department of Electrical and Computer Systems Engineering, Faculty of Engineering, Monash University, Clayton 3800, Victoria, Australia

[4]Department of Materials Engineering, Faculty of Engineering, Monash University, Clayton 3800, Victoria, Australia

[5]Research School of Engineering, College of Engineering and Computer Science, Australian National University, Australia

[6]FUNSOM and Collaborative Innovation Center of Suzhou Nano Science and Technology, Soochow University, Suzhou 215123, P. R. China

† These authors contributed equally to this work

* To whom correspondence should be addressed. A/Prof. Wenlong Cheng, Department of Chemical Engineering, Monash University, Clayton 3800, Victoria, Australia. Tel: +61 3 9905 3147; Email: wenlong.cheng@monash.edu
Webpage: http://users.monash.edu.au/~wenlongc/

Table of Contents

Section I Giant Plasmene Nanosheets

I-1 Synthesis and characterization of monodispersed NC nanoparticles

I-1.1 Synthesis of CTAC-capped gold nanospheres

CTAC-capped gold nanospheres were prepared using the seed-mediated growth method in a two-step procedure.[1-3] The first step involved the preparation of a brownish seed solution by mixing ice cold 0.6 ml 0.01 M $NaBH_4$ with an aqueous solution of CTAB (5 ml, 0.1 M) and $HAuCl_4$ (5 ml, 0.5 mM). The seed solution was then aged at 27°C for 3 hours. Then a growth solution was prepared by mixing 6 ml 0.5 mM $HAuCl_4$, 6 ml 0.2 M CTAC and 4.5 ml 0.1 M ascorbic acid. To grow CTAC-capped gold nanospheres, 0.3 ml of the as-prepared seeds were added into the above growth solution, which turned red almost immediately after mixing. The final solution was allowed to age for 1 hour followed by two cycles of centrifugation (14,500 rpm, 30 min) and finally re-dispersed into Milli-Q water.

I-1.2 Synthesis of CTAC-capped Au@Ag NCs

Typically, 0.5 ml of the CTAC-capped nanosphere was mixed with 4.5 ml aqueous CTAC solution (20 mM) and heated at 60°C for 20 minutes under magnetic stirring. Then the equal volumes (5 ml) of 2 mM $AgNO_3$ and AA-CTAC solution (containing 50 mM ascorbic acid and 40 mM CTAC) were simultaneously injected into the above heated solution at a rate of 0.2 ml min^{-1}. A color change from red to yellowish brown was observed during the injection. After dripping, the reaction was further allowed to proceed at 60 °C for 4 hours before cooling in an ice bath to stop the reaction. The Au@Ag NCs were finally washed once with water by centrifugation at 14,500 rpm for 15 min. The volumes of $AgNO_3$ and AA-CTAC solution were varied from 2ml, 5ml and 10 ml for different Ag thickness.

I-1.3 Characterization of CTAC-capped Au@Ag NCs

Fine-tuning sizes of Au@Ag NCs

Table S1 Dimension of synthesized Au@Ag NCs

Entry	Diameter [b] (nm)	-
Au nanosphere (core)	11 ± 1	-
Entry [a]	Length [b] (nm)	Thickness [b] (nm)
Au@Ag NC 1	21 ± 2	5
Au@Ag NC 2	28 ± 2	8.5
Au@Ag NC 3	33 ± 2	11

a: The ligands for all the nanoparticles were thiol-functionalized polystyrene (Mn=50,000, M_w/M_n *= 1.06); b: Obtained from TEM images of Au@Ag NCs, and statistical analysis through the free software ImageJ.*

Optical properties of Au@Ag NCs

By fine tuning the silver coating thickness of the Au@Ag NCs, it substantially influenced the overall optical responses (Figure S1). The Au@Ag NCS exhibited four characteristic peaks, and the nature of the plasmon modes were identified by performing near-field calculation of electric field intensity to evaluate E-field distribution in and around the nanoparticle. Bulk permittivity values of gold and silver in Au@Ag NCs were obtained from the literature.[4] Peak I can be ascribed to edge associated plane octupolar mode, peak II to an edge associated corner octupolar mode, peak III to a corner quadrupole mode, and peak VI to a corner dipole mode (Figure S2), similar to the ones reported in the literature[5]. With increasing shell thickness, the dominant peak corresponding to the longitudinal dipolar plasmon resonance mode was observed to redshift.

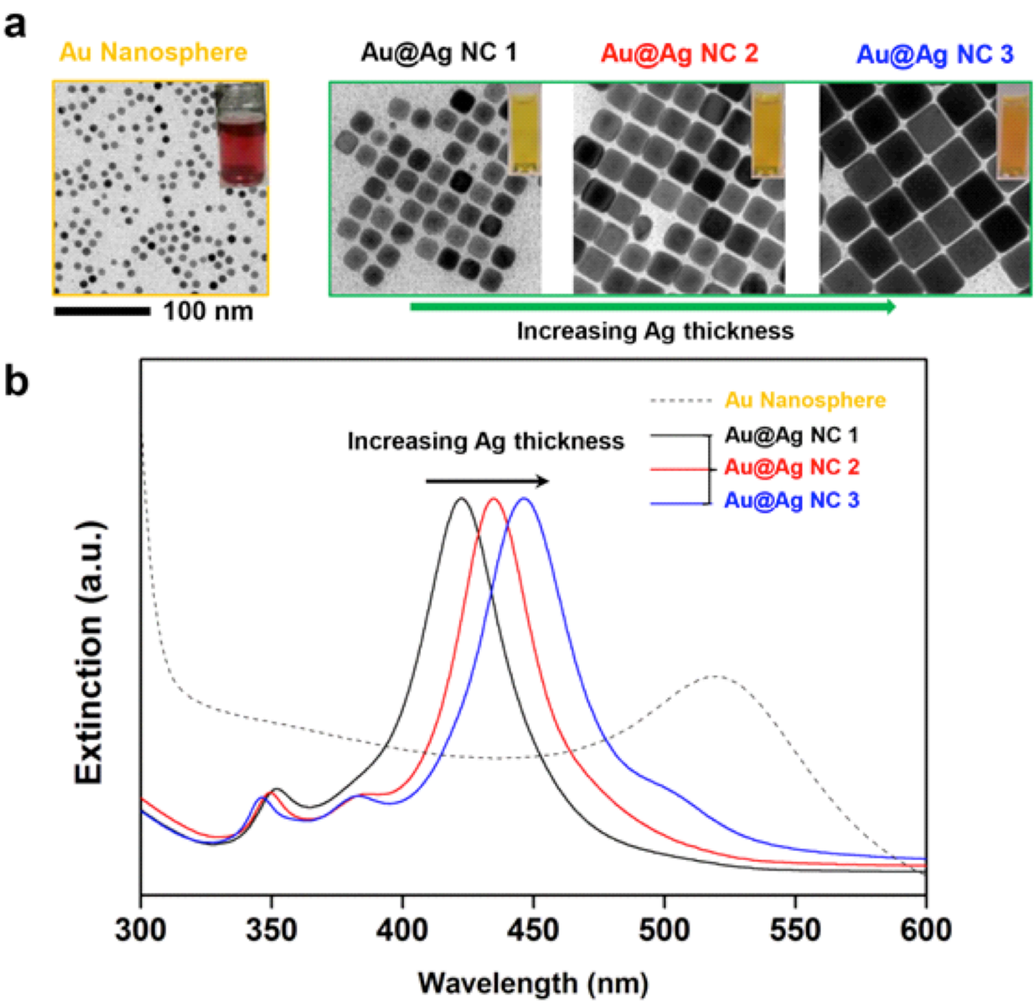

Figure S1. (a) TEM images of Au nanospheres and Au@Ag nanocubes with increasing thickness. (b) Extinction spectral development for Au@Ag NCs as silver thickness increases.

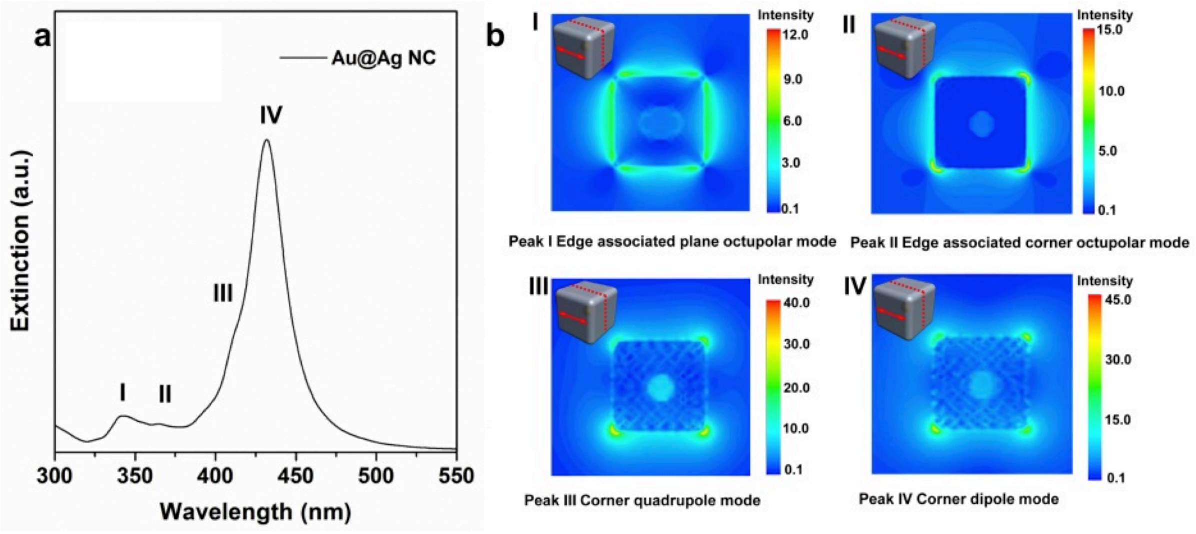

Figure S2. (a) Numerically calculated extinction spectrum of Au@Ag NC. (b) Calculation of near-field intensity distribution to evaluate electric field distribution of a single Au@Ag NC, when incident light is polarized along the direction shown in the insets. Electric field distribution represents the LSPR modes corresponding to the four plasmon resonance peaks.

I-2 Characterization of Giant Plasmene Nanosheets

I-2.1 Optical Properties

The major contribution to the optical properties of the plasmene nanosheets was found to stem from the dipole-dipole coupling between the Au@Ag NCs. Both experiment and simulation results showed that the resonant peak in the spectrum of NC plasmene exhibited a very minor red shift with increase in silver coating from 5nm to 11 nm (Figure S3).

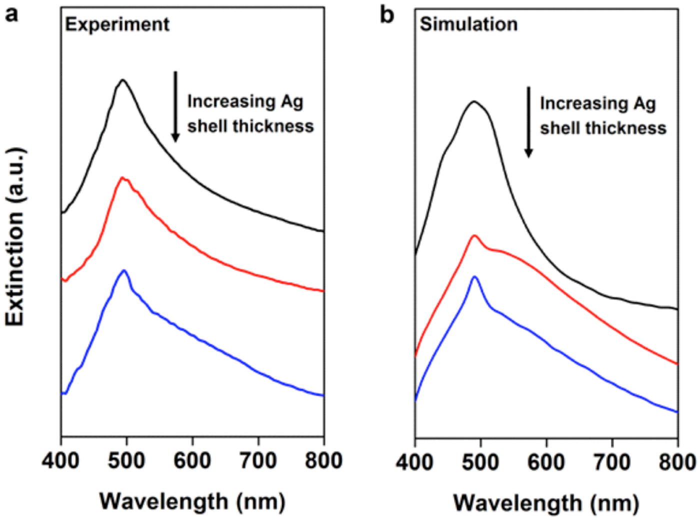

Figure S3. (a) Experimental and (b) simulated extinction spectra for NC plasmene nanosheets with increasing Ag shell thickness form 5 to 11nm.

I-2.2 Mechanical Properties

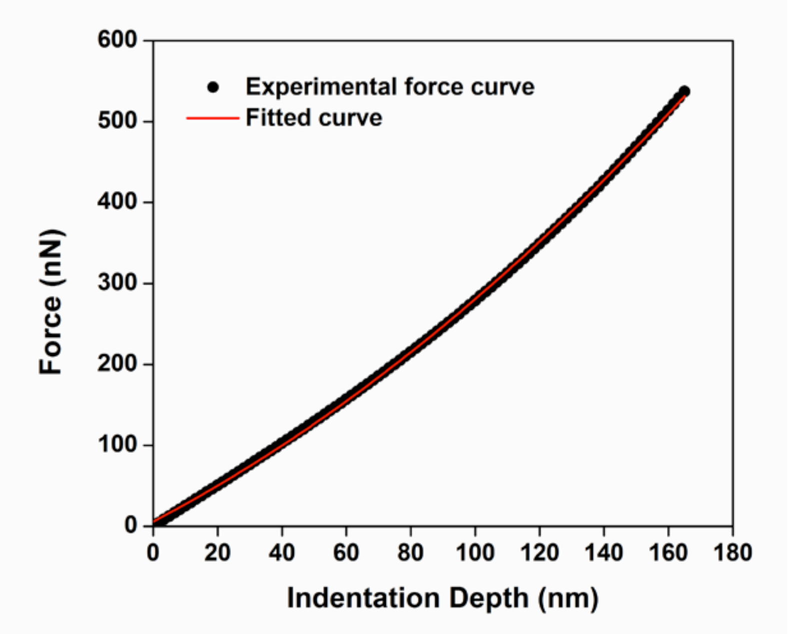

Figure S4. A typical force-displacement curve from AFM indentation (black) and from theoretical fitting (red) for NC plasmene nanosheet.

To measure the resonance properties, a 300 nm thick silicon nitride film is deposited on a double side polished Si wafer (crystal orientation of 100, thickness of 400 μm) via Low Pressure Chemical Vapor Deposition (LPCVD). The film is then subjected to photolithography and nitride reactive ion etching process to open a square-shaped window on the back side nitride film. PS-capped nanoparticles were then transferred to the substrate via a Langmuir-Schaefer technique.

These membrane resonators, with size in the range of 47-160 μm, show fundamental resonance frequencies in the range of 220-40 kHz (Figure S5). The membrane was calculated to have area mass density of 2.44×10^{-4} kg/m^2, with an estimated membrane tension of 0.050±0.006 N/m. The quality factor Q, which is proportional to the ratio of maximum energy stored in the device to the energy dissipated per cycle, was measured to be above 100 in air. This means the membrane has much lower viscous damping in air, compared with Au nanoparticle drum resonators. These Q values could be enhanced further in vacuum, by eliminating air damping.

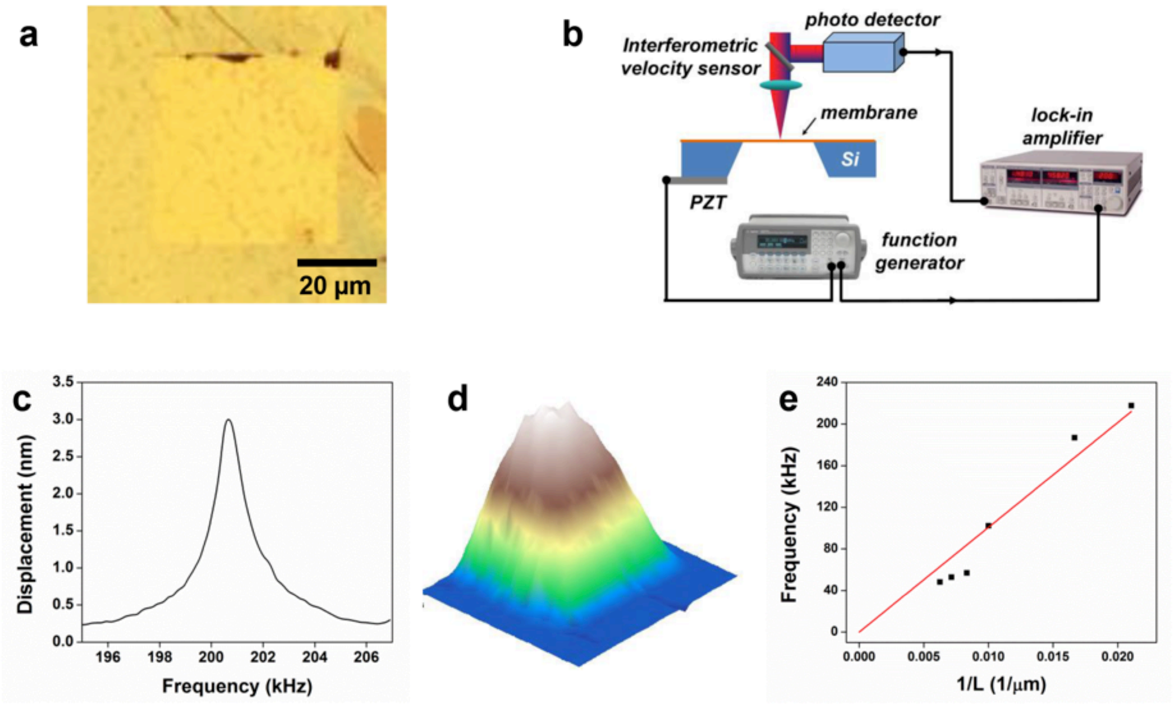

Figure S5. (a) Microscope image of a typical suspended plasmene membrane. (b) Schematic illustration of the experimental set up for the membrane resonator characterization. (c) Measured mechanical vibration *Displacement vs Driving Frequency* of the fundamental resonance mode of a square shaped membrane resonator, with membrane size L = 47 μm. The PZT driving amplitude was 10mV. This mode shows a quality factor of 133. (d) A measured standing wave pattern of the fundamental resonance mode in (c), which is a contour plot of the vibration displacements for the whole membrane. (e) Measured fundamental resonance frequency of various membranes with different sizes. These resonance frequency measurements were carried out in air.

I-3 Surface Propagating Plasmons

I-3.1 Exact modelling of surface plasmon propagation

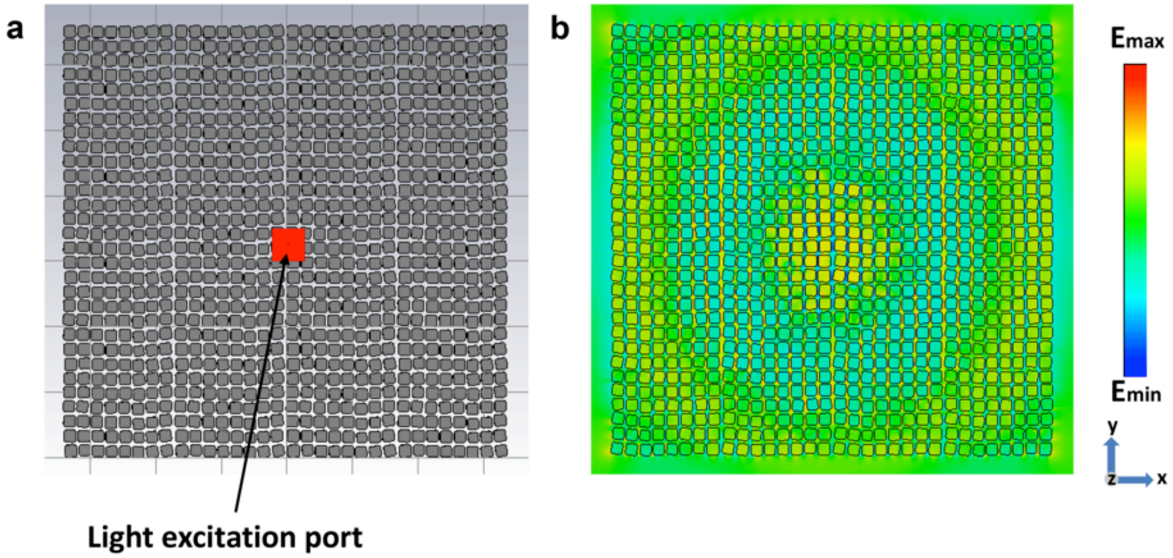

Figure S6. Electric field distribution of the surface propagating plasmons on a 2D NC plasmene sheet (~1.4 × 1.4 μm^2) , showing patterns of cylindrical surface waves analogous to that found on graphene surfaces. (a) Surface plasmons are excited in the center of the plasmene sheet using excitation from the port (red square). (b) These plasmons propagate radially outwards which can be further visualized in the Supporting Movie 1 and 2.

I-3.2 Time-domain study of surface plasmon modes

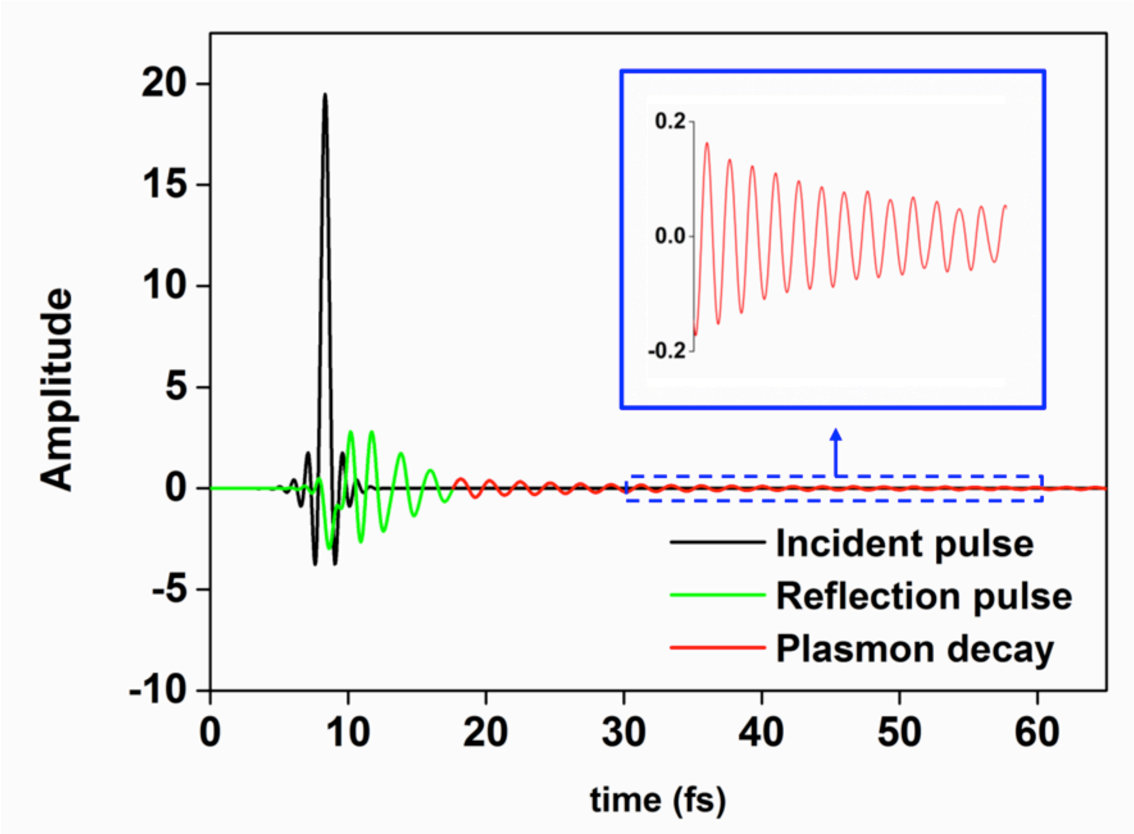

Figure S7. Simulated electromagnetic response of a NC plasmene sheet. After subjecting to incident light (black), light is reflected (green) and coupled in to a decaying plasmon resonance (red). Inset shows the magnified tail end amplitude for clarity.

I-3.3 Experimental observation TM-only propagating plasmons

Figure S8 schematically shows the experimental configuration of the polarization measurements. A linear polarized (45°to the left) Nd:YAG 532 nm laser was introduced into the fiber bench which was equipped with a quarter wave-plate and linear polarizer. The quarter wave-plate converts the linear polarization into circular polarization. By rotating the angle of the linear polarizer after the quarter wave-plate, linear polarization of light can be changed to a desired angle, which is fed into a D-shaped optical fiber covered with samples. The D-shaped fiber is precisely polished into fiber core to enhance the interaction between the evanescent fields and the sample. The output signal from the fiber-to-plasmene nanosheet coupler was then detected by an optical power meter PM120D (Thorlabs) with a resolution of 1 nw. 2D plasmene nanosheet was transferred to the fiber with assistance of PDMS. The insertion loss of side-polished optical fiber at telecommunication wavelength was measured to be ~ 7 dB and insertion loss of fiber bench to be ~ 1.7 dB. Thus, the total insertion loss of the measurement system is ~ 8.7 dB.

Reference experiment and polarization experiment were performed on the as-prepared fiber and fiber decorated with 2D plasmene sheet. The polarization extinction ratio (PER) in dB,[6, 7] the ratio of optical powers between the orthogonal polarized light, was given by

$$PER = 10\log\left(\frac{Py}{Px}\right) \tag{1}$$

where Py and Px stands for the measured power in both y and x polarization. Figure S9 shows the polar image of the output power from the fiber-to-plasmene coupler as a function of the polarization angle. According to above formula, we can get a PER of 10.29 dB. The maximum output occurred at θ= 90°, and the minimum appeared at θ= 0°, confirming the p-polarized nature of transmitted light. The extinction ratio is comparable to the solid metal film based polarizers.[8] The origin of this polarization effect is that the optical photons are selectively coupled into surface plasmon polaritons which are vertically polarized and propagate through the plasmeme sheet, and the surface plasmon polaritons are further coupled back into p-polarized optical photons after the plasmene. In comparison, the s-polarized optical photons are not supported due to the limit of the boundary conditions at plasmene-fiber interface and will be scattered into the fiber cladding.

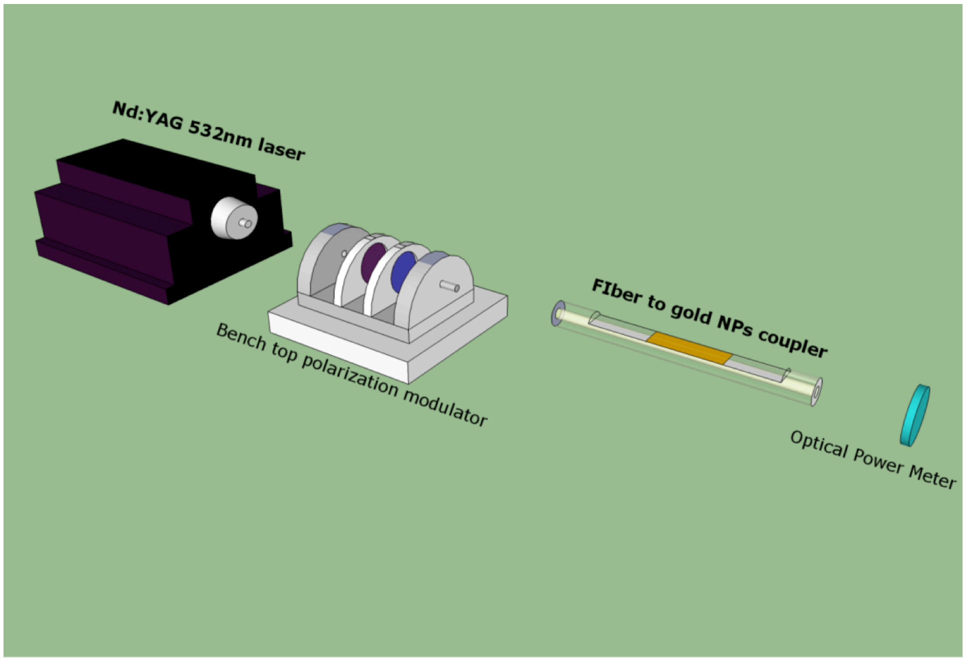

Figure S8. Experimental configuration of the polarization measurements on fiber-to-plasmene nanosheet membrane coupler.

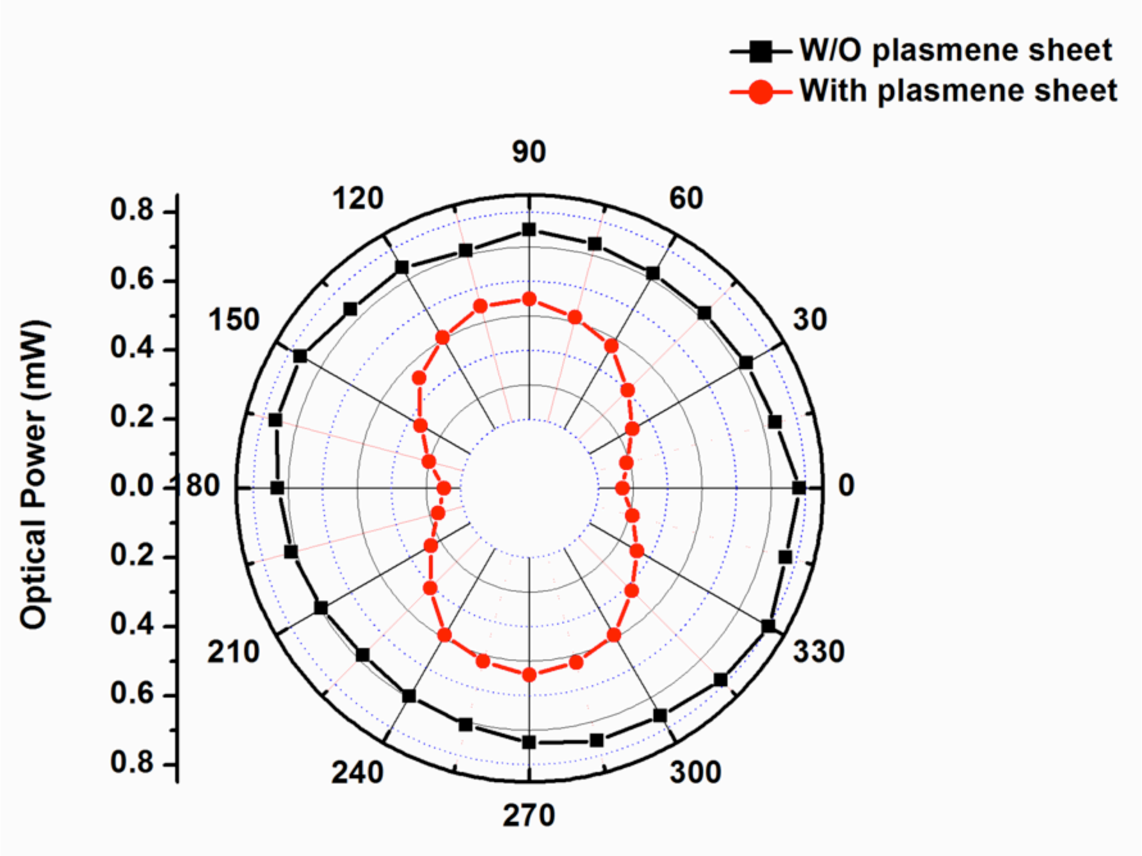

Figure S9. Polar image measured at 532 nm from specially polished D-shape fibers with/without plasmene sheet

Section II Plasmene Nanoribbons

II-1 FIB Fabrication of plasmene nanoribbons

Patterning of plasmene nanosheets into plasmene nanoribbons was performed using FIB milling with operating voltage of 30kV and ion beam current of 28 pA. Figure S10 illustrates the scheme for the patterning of a nanoribbon, which is formed by creation of two slots. The slot lengths and gaps are designed depending on the required length and width of the nanoribbon, which has been demonstrated down to ~100nm wide. One critical step is to minimize any lateral stresses on the ribbons during milling as to avoid causing bending/damaging to the ribbons.

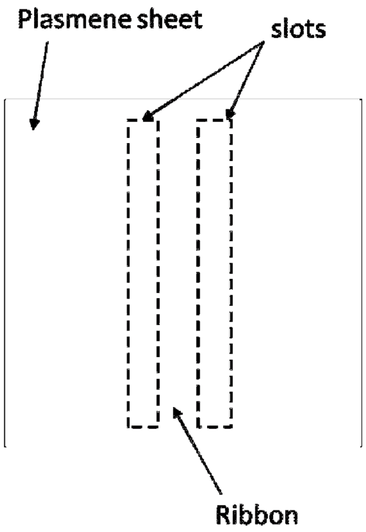

Figure S10. Scheme for FIB nanoribbon patterning. The dotted patterns are the two slots which are to be milled away, producing a nanoribbon.

II-2 Width-dependent plasmonic properties of nanoribbons

We further investigate on the width-dependent plasmonic properties of the plasmene nanoribbon and analyze the modes associated with the peaks of the extinction spectra in Figure 3f. In numerical simulation of these spectra we assumed an idealistic scenario, where all NCs in a ribbon are identical in size (length of 33 nm) and uniformly separated from its neighbors (spacing of 12 nm). The nanoribbons were considered to have a length of around 3.4 μm, nearly identical to the length over which the experimental spectra were obtained. The breadth of the nanoribbons were varied by placing 3, 4, 6, 8 and 11 NCs along the width, which corresponds to nanoribbon widths of 135, 180, 270, 360, and 495 nm respectively.

We consider the surrounding medium of the nanoribbons to have a refractive index of 1.55, close to that of PS. Figure S11 shows the distribution of E-field for a 3-NC wide plasmene nanoribbon along the z-plane passing through the center of the particles, which correspond to the peaks i, ii, and iii respectively. Notice that, besides the pattern of the near-field, the comparison of the absolute values of the E-field at these peaks indicates that peak iii is the most dominant one.

Further, we thoroughly investigate the origin of all the peaks seen in the spectra (Figure 3f) of plasmene nanoribbons having different widths. Electric field distribution patterns (Figure S11) indicate that the peaks i, ii, and iii can be attributed to edge-coupled, corner-coupled, and edge-corner coupled modes, respectively. Beside these dominant peaks, each spectrum also features a few more minor peaks at wavelengths longer than that of the peak iii. The origin of these peaks can be understood from the mode of interaction between NCs along the length of nanoribbon, as they may vary with the width of the ribbon.

Electric field-lines pattern for each mode is presented in Supplementary Figure S12. It can be observed that the peaks at energy higher than that of the dominating peak, namely peak i and ii, arise mainly because of coupling between higher orders multipolar modes. The dominant peak (peak iii) can be attributed to symmetrical dipolar coupling, which gets stronger as the width of the plasmene nanoribbon increases. For different nanoribbon width under consideration, the nature of peaks i, ii, and iii remains unchanged. However, different low energy peaks evolve with change in nanoribbon width, which is further investigated.

For a 3-NC wide nanoribbon, a minor shoulder peak (peak 3.iv) is observed at lower frequency than the dominant peak 3.iii, and this peak can be attributed to antisymmetric coupling mode. As the ribbon width increases to 4-NCs, the antisymmetric coupling mode gets stronger and redshifted (peak 4.v). An additional peak (peak 4.iv) appears next to the symmetrically coupled peak 4.iii, which can be ascribed to a weakly coupled symmetrical mode. For a 6-NC-wide nanoribbon the antisymmetric mode gets further redshifted and enhanced (peak 6.v), however the spectral position of the weak symmetrically coupled mode (peak 6.iv) remains almost same as that for peak 4.iv. With further increase in ribbon width to 8-NCs, this mode (peak 8.iv) is still observed at the same position, but notice that the peak shows a diminishing trend with increase in ribbon width (compare peaks 4.iv, 6.iv, and 8.iv). However, the antisymmetric coupled mode gets further redshifted (peak 8.vi), but weakens and gives rise to an additional peak of another antisymmetric-type coupling (peak 8.v) at higher energy than that of peak 8.vi. At ribbon width of 11-NCs, the two antisymmetric modes get further apart, where the low-energy antisymmetric mode gets red-shifted (peak 11.v) and high-energy antisymmetric mode is blueshifted (peak 11.iv).

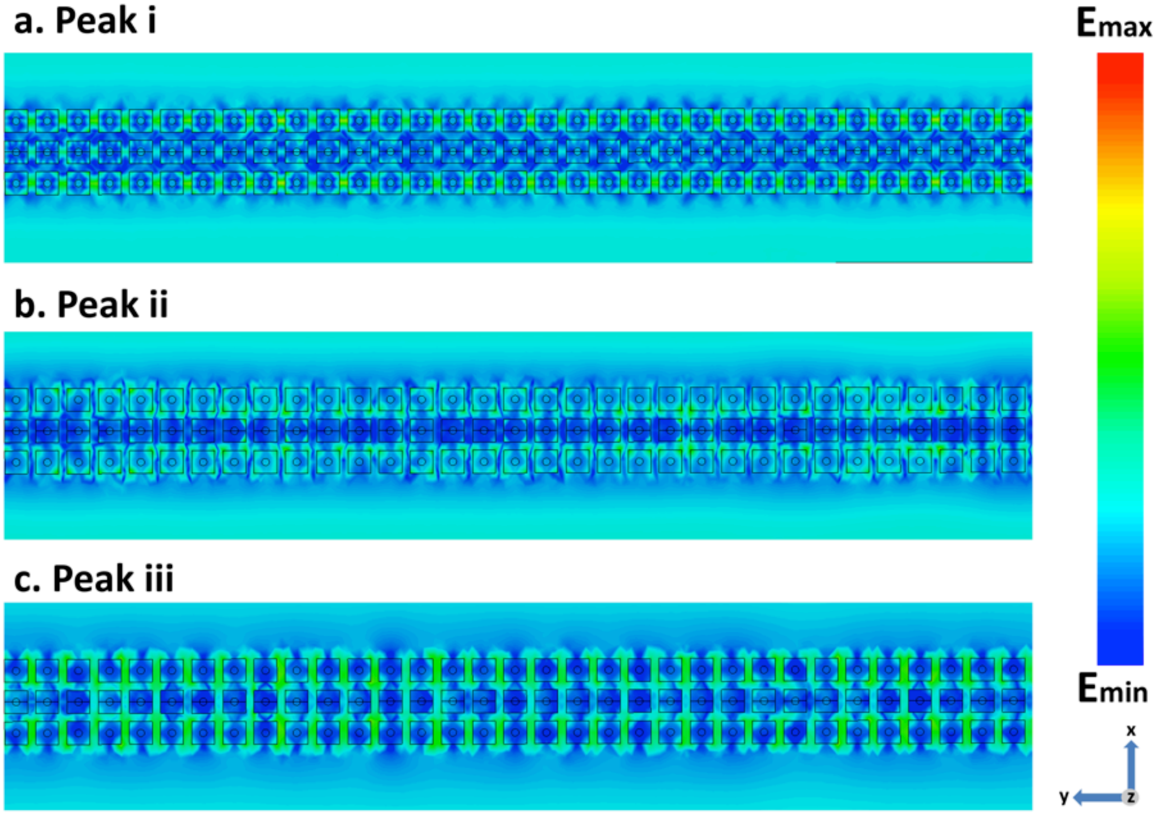

Figure S11. Electric field distribution for 3-NC wide plasmene nanoribbon with light polarized along the y-direction. (a) Peak i is attributed to the *edge coupled* mode; (b) peak ii is attributed to the *corner coupled* mode; (c) peak iii is attributed to the *edge-corner coupled* mode.

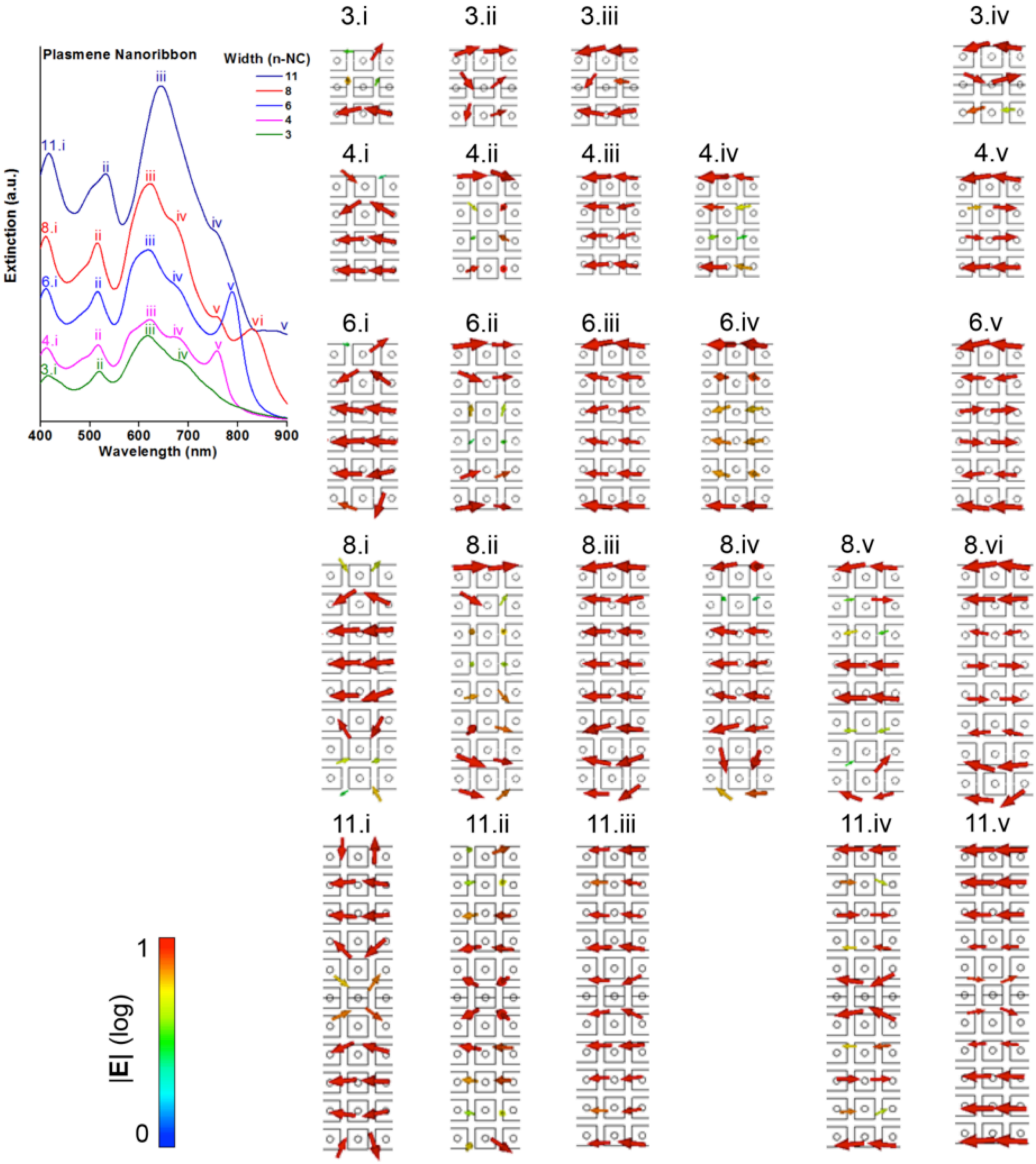

Figure S12 Electric field-lines pattern for each spectral peak seen in the extinction spectra of plasmene nanoribbons with varying width. For each spectrum, the peaks are enumerated and their corresponding E-field line patterns are extracted from the same section of the nanoribbons.

Section III Plasmene Origami

III-1 Mechanism of FIB-induced folding

Our approach to automatic self-folding employs ion beam etching of soft polystyrene ligands on a homogenous plasmene sheet to induce stresses responsible for folding. Ion-polymer interactions as a result of bombardment of high energy gallium ions on the surface PS ligands contribute to localized heating. This promotes bond cleavage and subsequent monomer evaporation forms the nanoparticle surfaces. The partial removal of ligands then destabilizes the interactive nanoscale forces, in which additional van der Waals attraction between the etched nanoparticle core lead to a folding effect (Figure S13).

III-2 Fabrication of origami by programmed FIB lithography

The self-folding mechanism can be programmed in a way that 3D origami structures can be formed by using sequential steps (Figure S14). Figure S15 – S19 shows the sequential steps to pattern a 2D plasmene sheet into different 3D origami structures. The design and folding of such origami structures generally involves two steps. The first is to mill a nanoribbon with the desired cross sectional area, followed by localized partial etching at predesigned locations for sequential folding into the desired origami structure. The successful folding of these structures is primarily governed by the dwell time and gallium ion dosage. The dwell time used in this study is fixed at 100 μs for cutting through and 100 ns for inducing folding. The Ga^+ ion dosage in ions/cm^2 can be calculated according to:[9]

$$Ion\ dosage = \frac{I_{ion} \times t_{mill}}{A_{mill} \times 1.602 \times 10^{-15}} \tag{2}$$

where I_{ion} is the ion beam current in pA, t_{mill} is the dwell time in s and A_{mill} is the pattern area in μm^2.

We investigated the folding approaches with varying dosage of gallium ions at an accelerating voltage of 30kV. The optimal ion dosage was determined to be ~10^{11} ions/cm^2, in which 3D origami structures can be cut and folded in less than 10 seconds. As expected, similar structures can be reproduced at a lower dosage of ~10^9 ions/cm^2, but a significant increase in amount of milling time is required. At a high ion dose of ~10^{16} ions/cm^2, it causes substantial damage to the plasmene sheets. In addition, the folding angle generated can be controlled up to 90^o depending on the depth of ion milling.

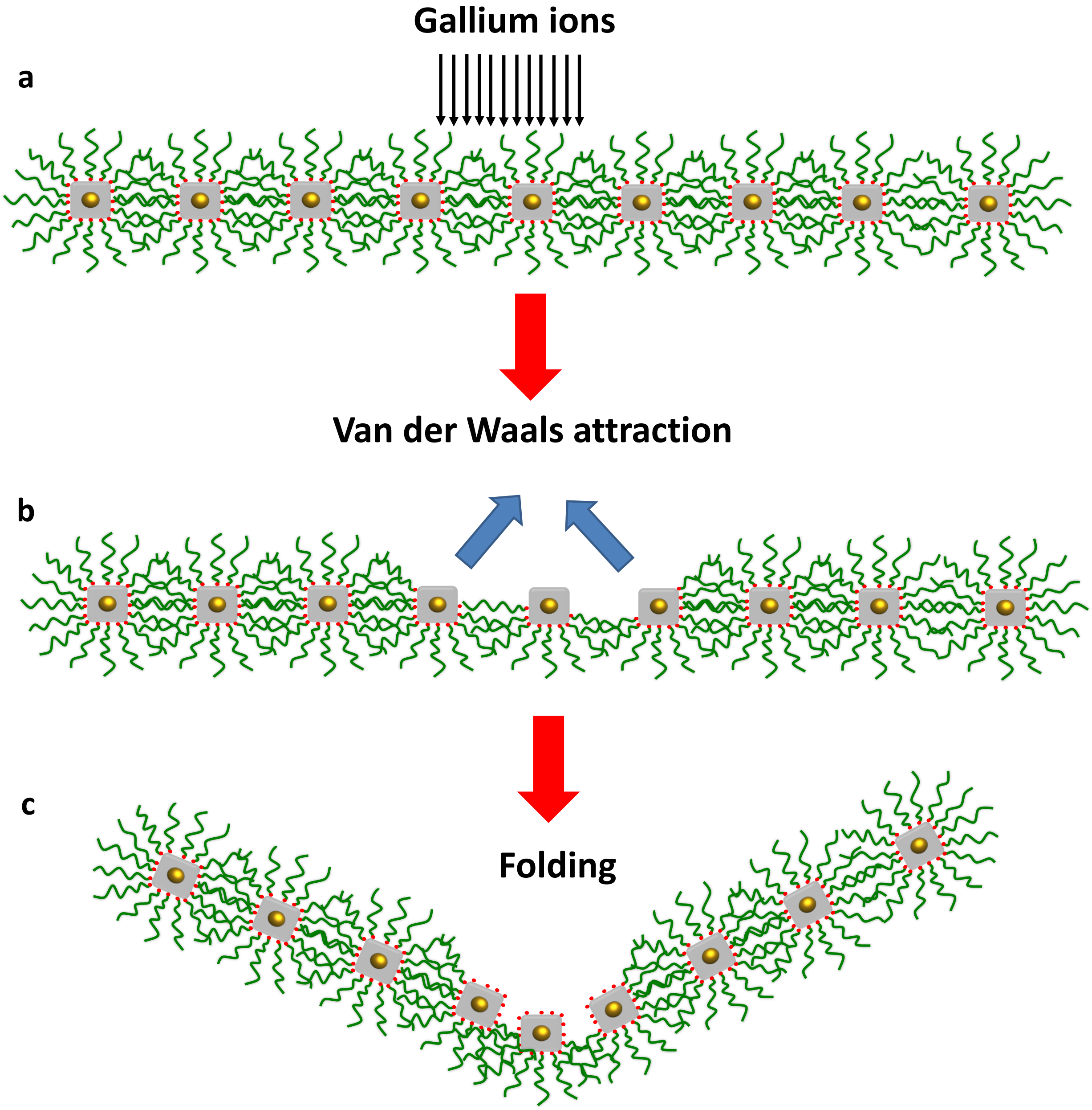

Figure S13. (a) Bombardment of high energy gallium ions onto assembled plasmene sheets. (b) Partial etching of surface polystyrene ligands resulted in additional van der Waals attraction from the nanoparticle core. (c) Folding of the plasmene sheet.

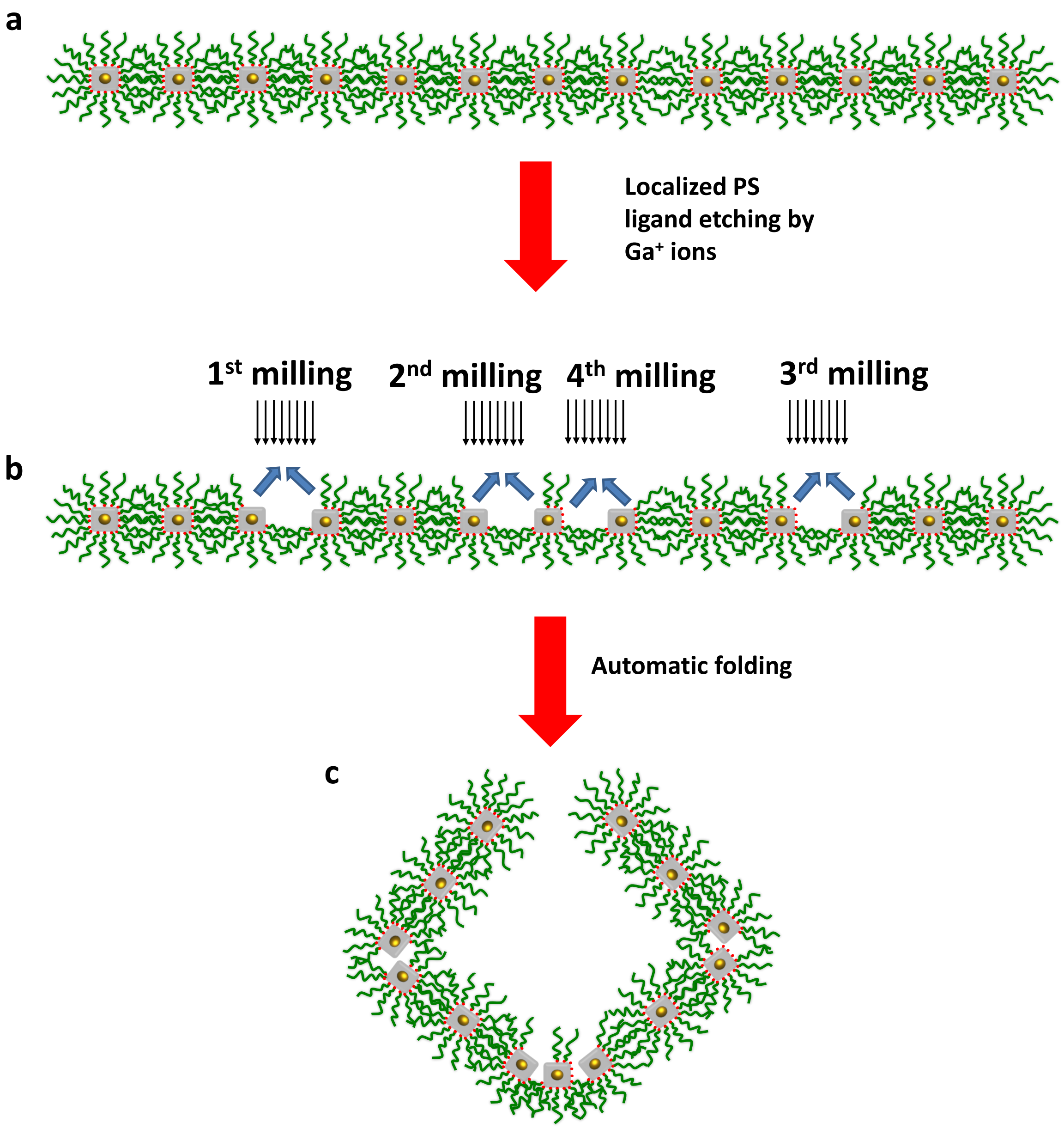

Figure S14. Schematics showing the sequential milling of a plasmene nanoribbon into a cubic origami

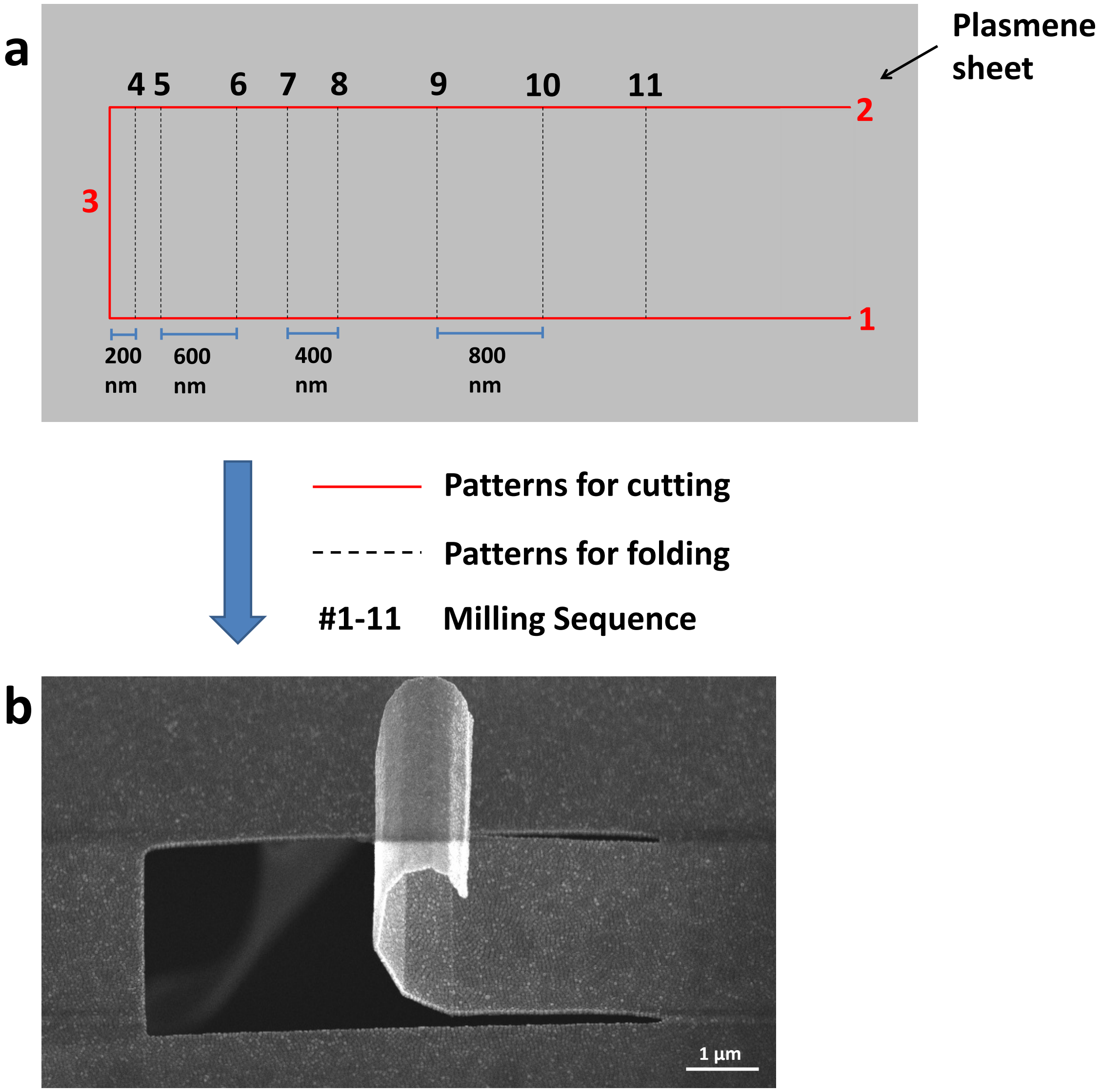

Figure S15. (a) Sequential steps for patterning a rolling nanoribbon. Red lines indicate cutting through of the plasmene sheet to get a nanoribbon. Black lines indicate the partial etching to induce folding. The numbers indicate the sequence for milling. (b) Corresponding SEM image of the rolling nanoribbon

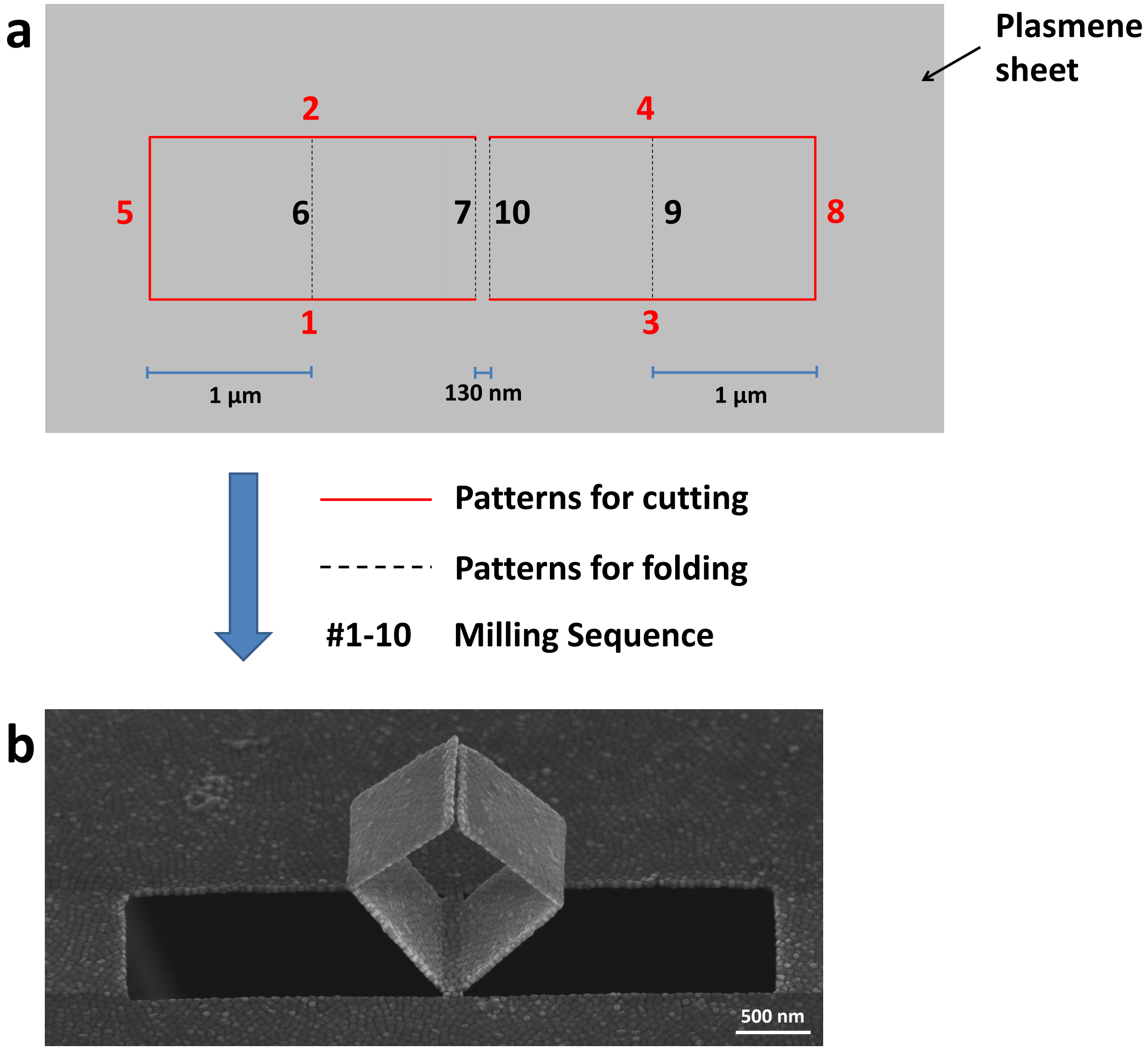

Figure S16. (a) Sequential steps for patterning a cube origami. Red lines indicate cutting through of the plasmene sheet to get a nanoribbon. Black lines indicate the partial etching to induce folding. The numbers indicate the sequence for milling. (b) Corresponding SEM image of the 3D cube origami structure.

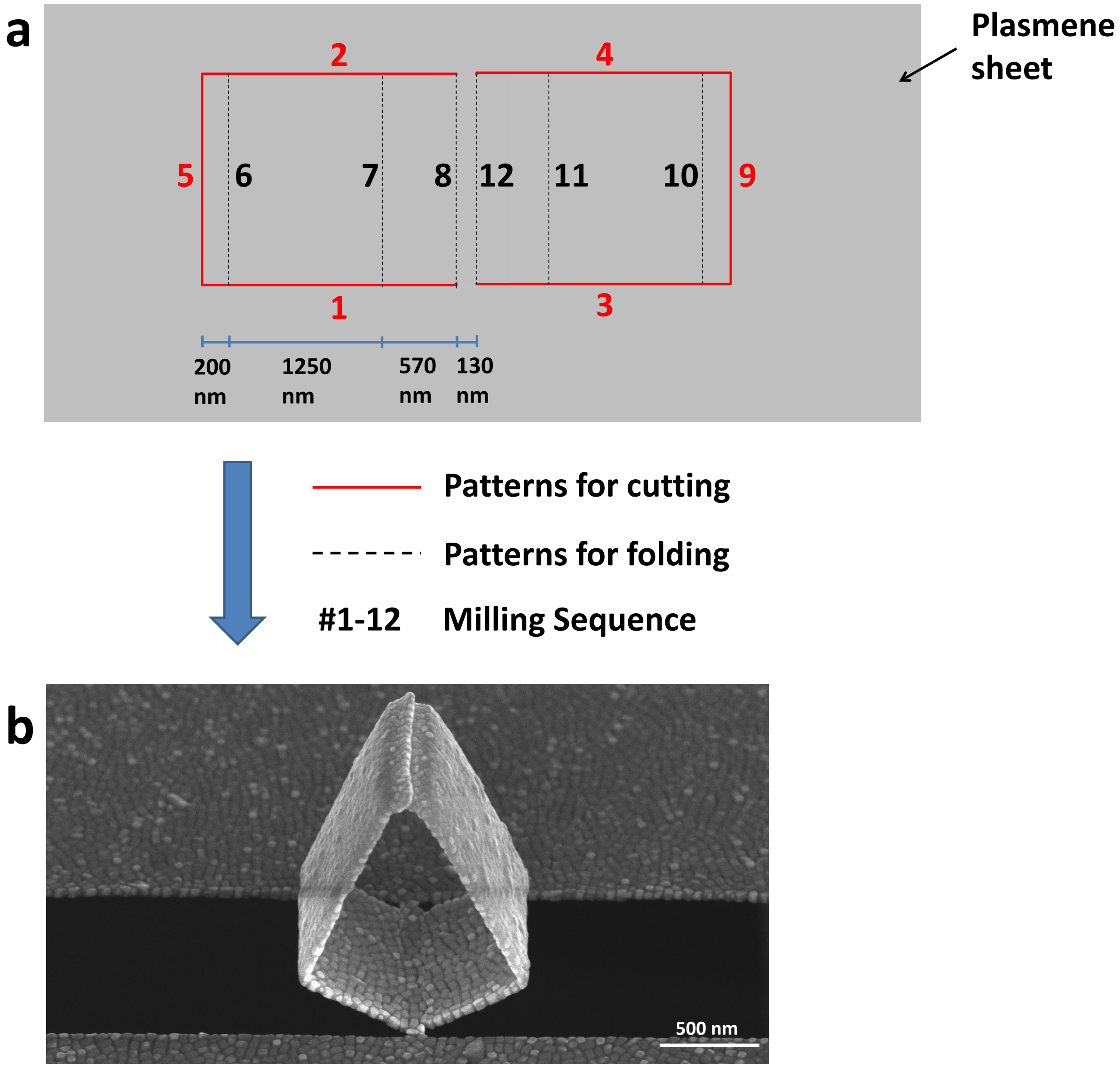

Figure S17. (a) Sequential steps for patterning a diamond origami. Red lines indicate cutting through of the plasmene sheet to get a nanoribbon. Black lines indicate the partial etching to induce folding. The numbers indicate the sequence for milling. (b) Corresponding SEM image of the 3D diamond origami structure.

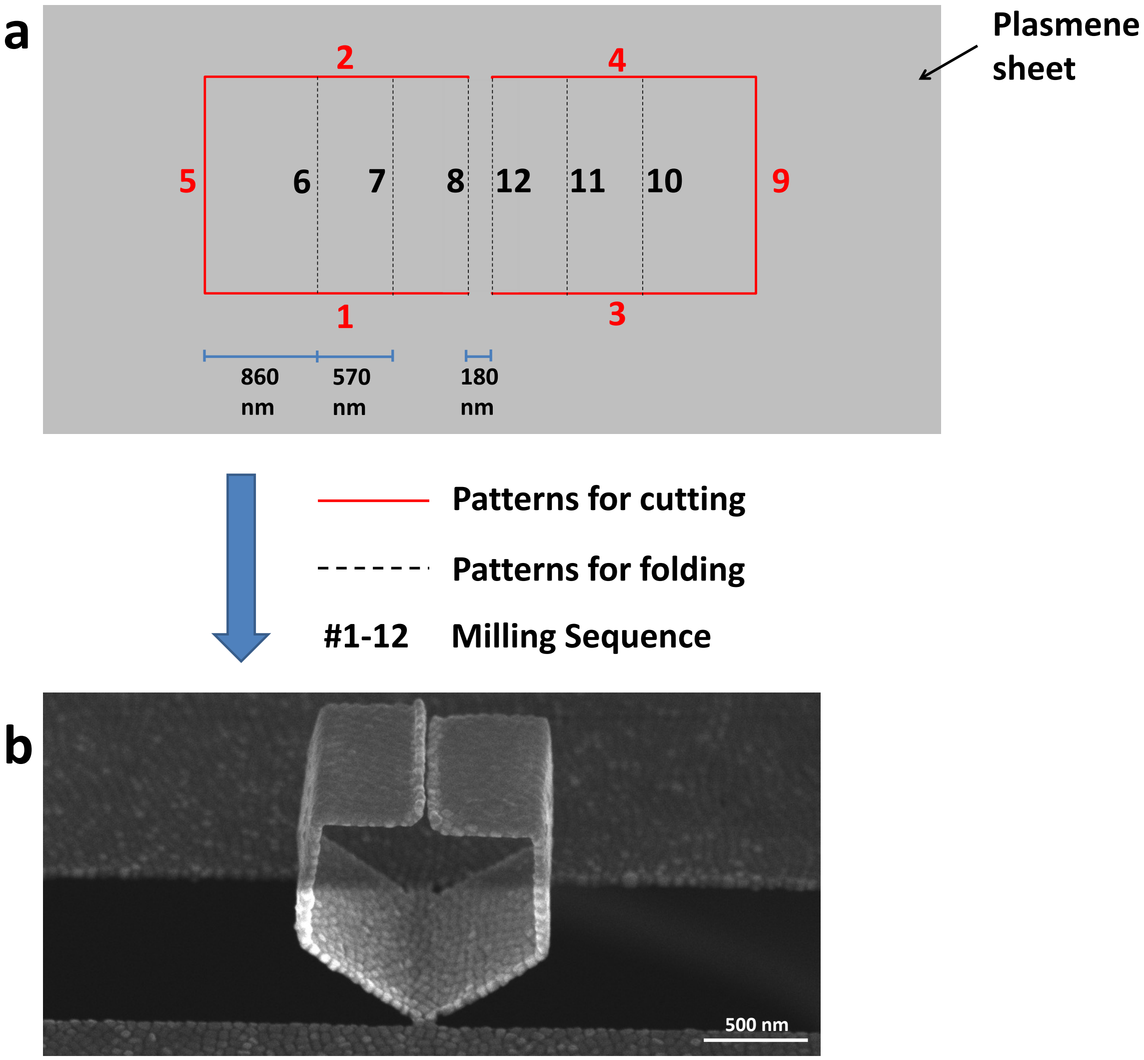

Figure S18. (a) Sequential steps for patterning a pentagon origami. Red lines indicate cutting through of the plasmene sheet to get a nanoribbon. Black lines indicate the partial etching to induce folding. The numbers indicate the sequence for milling. (b) Corresponding SEM image of the 3D pentagon origami structure.

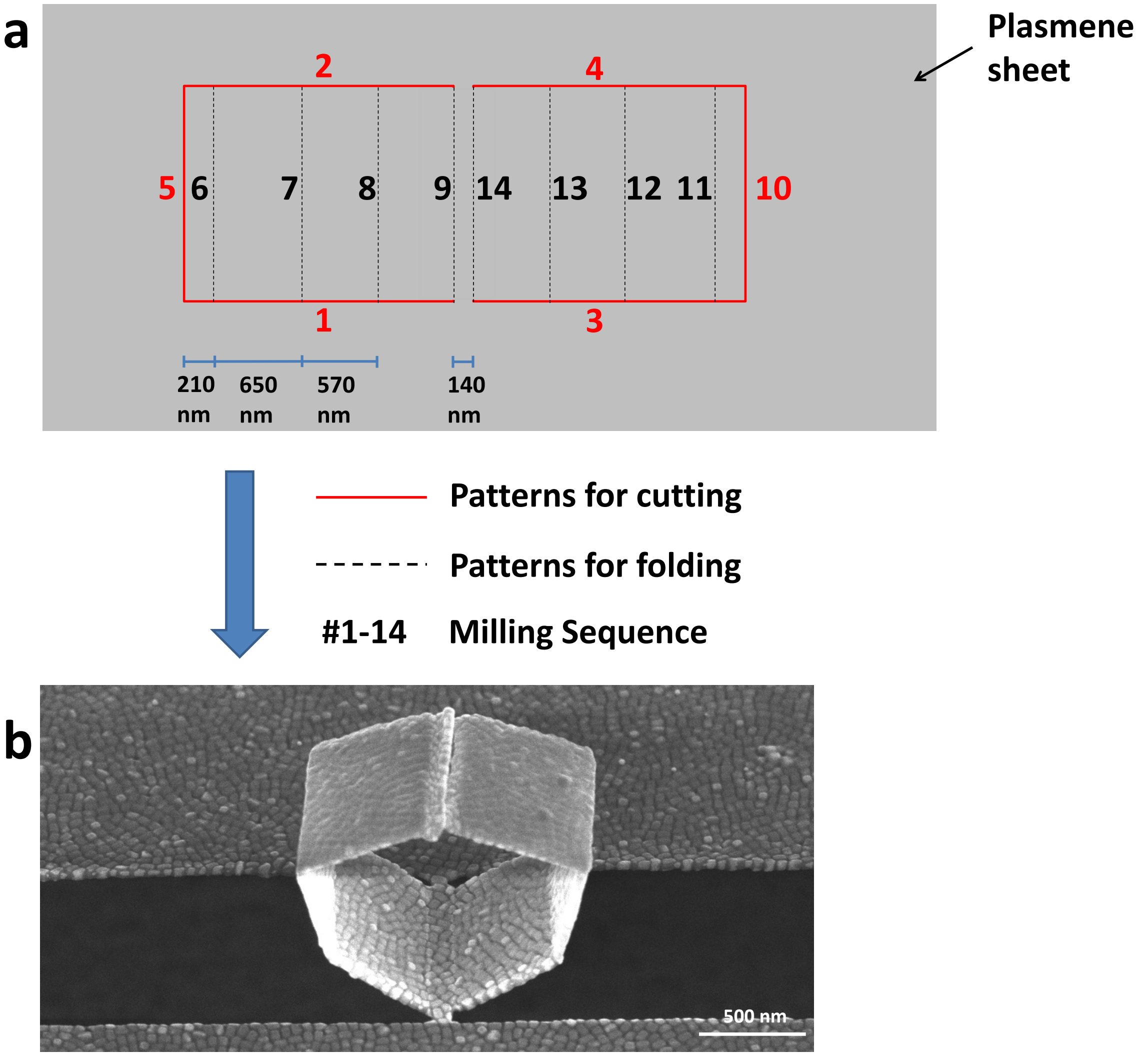

Figure S19. (a) Sequential steps for patterning a hexagon origami. Red lines indicate cutting through of the plasmene sheet to get a nanoribbon. Black lines indicate the partial etching to induce folding. The numbers indicate the sequence for milling. (b) Corresponding SEM image of the 3D hexagon origami structure.

III-3 Numerical Modelling: how folding affects plasmonic properties

The effect of folding of a plasmene nanoribbon on its optical response is systematically studied by numerically evaluating the extinction spectra for folding angles of 15º, 30º, 45º, 60º, and 75º (Figure S20). Folding of nanoribbon is schematically shown in 2D (Figure S20 (i)) and 3D (Figure S20 (ii)), and the optical response of the folded ribbons are plotted in Figure S20 (iii). We calculated the extinction spectrum of the nanoribbons, with a simplifying assumption that each nanoribbon is an array of NCs with identical sizes and identical interparticle spacing, as mentioned in the section II-2. The width of the ribbon was around 495 nm (i.e., of 11-NC) and its length was about 1.45 μm (as measured experimentally).

The overall trend of the spectral shift of the dominating peak with increasing folding angle is highlighted using blue-dotted curved line in Figure S20 (iii). Note that the spectrum corresponding to 0º belongs to the .unfolded nanoribbon, which features two main peaks (marked as ‘a’ and ‘b’) with mode ‘b’ being the dominating one. Electric-field distribution pattern corresponding to these peaks are shown in Supplementary Figure S21. With 15º folding, peak ‘a’ strengthens and exhibits red shift, while peak ‘b’ undergoes a minor blueshift. E-field pattern for these modes in Figure S21 also shows that mode ‘b’ is the dominating one. At folding angle of 30º, a new low energy peak ‘c’ arises, while peak ‘a’ gets further enhanced and redshifted, and ‘b’ is blueshifted. At 45º both peaks ‘a’ and ‘c’ get redshifted and enhanced, whereas ‘b’ gets blueshifted and finally merged with mode ‘a’ at an angle of 60º, making ‘a’ to be the dominating peak of the spectrum. With further increase in folding angle, the trend follows — where peaks ‘a’ and ‘c’ got further redshifted due to increase in interparticle coupling between the nanoparticles of the two folded wings. Interesting to note that peak ‘a’ got stronger, whereas peak ‘c’ started showing trends of getting broader and weaker. The dashed and the dashed-dotted lines in Figure S20 (iii) help one to follow the spectral trend of red shift of the modes ‘a’ and ‘c’, respectively. Besides, the corresponding E-field patterns in each case (see Figure S21) also show that for folding angle of 60° and above mode ‘a’ becomes the dominating peak with relatively much larger near-field confinement and hence, exhibits much stronger absorbance.

It is known that for light incident from bottom, depending on the folding angle the phase of light reaching the nanoparticles at similar heights of different folded nanoribbons is going to be different. This essentially influences the collective resonance of the surface plasmons and hence, there is a shift in the resonance energy of a folded plasmene nanoribbon. For the folded nanoribbon structure shown in Figure S22, a cross-section in xz plane allows one to analyze the E-field distribution of the structure at a particular phase of the incident plane wave. The first column shows the cross-sections taken at half-height of the nanoribbon structures folded at angles of 15°, 30°, 45°, 60°, and 75°. These y-slices correspond to E-field distribution patterns excited at different phases of incident light. To observe the E-field distributions of folded nanoribbons (for different angles of folding) excited by light with a constant phase, we plotted the cross-sections of y planes at $\lambda/4$ and $\lambda/2$, where λ is the free space wavelength of the incident light. This shows how the number of interacting nanoparticles along a plane varies with folding angle, and the corresponding variation in near-field confinement pattern. E-field patterns for all the folded nanoribbons extracted along $z = 0$ plane are also shown in the rightmost column. All these allow one to compare and appreciate the changes in E-field distribution and confinement in a folded nanoribbon as a function of folding angle.

Furthermore, we numerically calculated the extinction spectra of the simulated 3D origami structure given in Figure 4d (similar to the fabricated one in Figure 4c). Simulation shows that the spectral position of the dominant peak is quite consistent with the one in experiment. Although, the fabricated nanoribbon had distributions in constituent NCs' sizes and spacings, leading to a much wider experimental spectrum (typically featuring one broad prominent peak), our simulation with simplifying approximations still closely can reproduce the spectral features.

The dimensions of the origami structure are given in Figure S23 (i). This closed 3D origami allows one to analyze the effect of multiple folding in the optical response of a plasmene nanoribbon. Note that in analyzing the optical response of such multi-folded structure, the folding angle of the nanoribbon's faces, on which light is incident upon, plays a major role (see Figure S20). The origami structure model (adapted based on the fabricated one) records the folding angle to be an acute angle of 60° (see Figure S23). This helps one to estimate that the optical response of the folded structure will be blue-shifted with respect to that of the unfolded nanoribbon (see 60° single folding case in Figure S20). In this case, beside the 60° fold, there are two additional folds, which bring the ends of the nanoribbon closer. This increases the interparticle interaction between the nanocubes at two ends of the ribbon, and hence such multi-folded structure exhibits a redshifted spectrum when compared to a single-folded nanoribbon with similar angle of folding.

The extinction spectrum shows that the dominant peak is at around 510 nm along with a few minor peaks/ shoulder peaks at spectral positions shown in Figure S23 (i). Figure S23 (ii) presents the normalized E-field distribution patterns at each peak location, showing that the strongest E-field confinement occurs at the position of extinction maximum 'b'. The absolute value of the maximum E-field in each case is plotted in Figure S23 (iii), which also helps appreciate that the maximum E-field enhancement takes place at 510 nm. Note that, in Figure S23 (ii) all the E-field distributions are obtained at $z = 0$ plane correspond to different wavelengths of the incident light. This allows one to compare and appreciate the variation in near field confinement with change in incident light wavelength (*i.e.*, with change in phase of E-field excitation at the same height of the folded structure). Note that, in the fabricated origami structure, owing to minor disordering and distribution in nanocube sizes and spacings, only the dominant peak prevails — giving rise to a wide spectrum with no clear evidence of the low energy secondary peaks/ shoulders.

Using similar approximations, we further simulated the optical response of cube origami structure (Figure S24), which has folding angle of 45°. We considered all sides to be of equal length (of around 360 nm) and width of the structure as 495 nm. Note that, the nanoribbon mentioned above (in Figure 4c) was folded to get the cube-like shape. We observe a blue-shift in the spectrum when compared with the unfolded ribbon's spectrum in Figure 4d (and Figure S23). However, the cube origami's spectrum is red-shifted as compared to that of the origami shown in Figure S23, which has the initial folding angle of 60°. This behavior is found consistent with the observations from the spectral trends of nanoribbon folding, as shown in Figure S20.

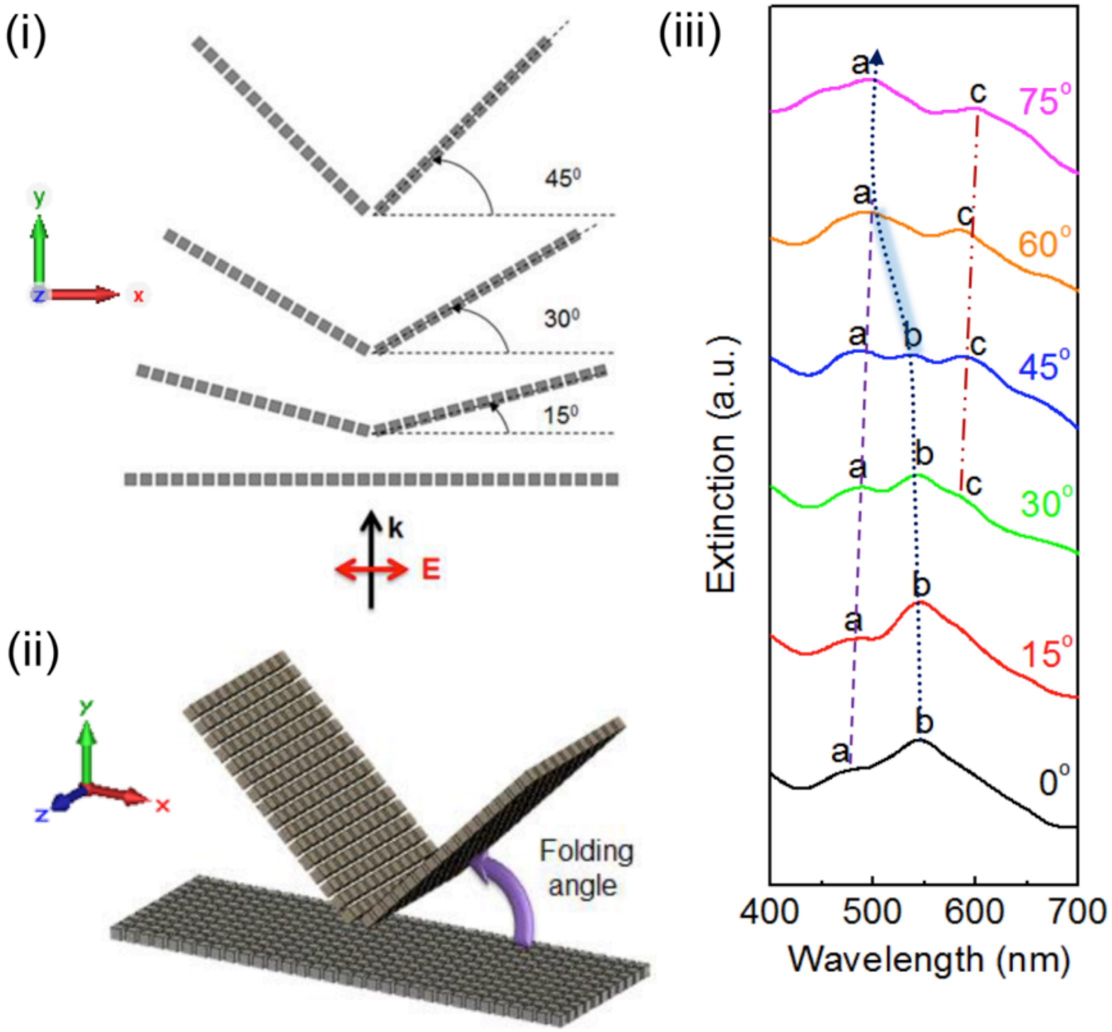

Figure S20: Folding of plasmene nanoribbons. Schematic representation of folding in (i) 2D and (ii) 3D, and (iii) the optical response of the folded nanoribbons. Incident light propagation (**k**) and polarization (**E**) directions are shown in (i). Note that individual spectra in (iii) are vertically offset for better viewing.

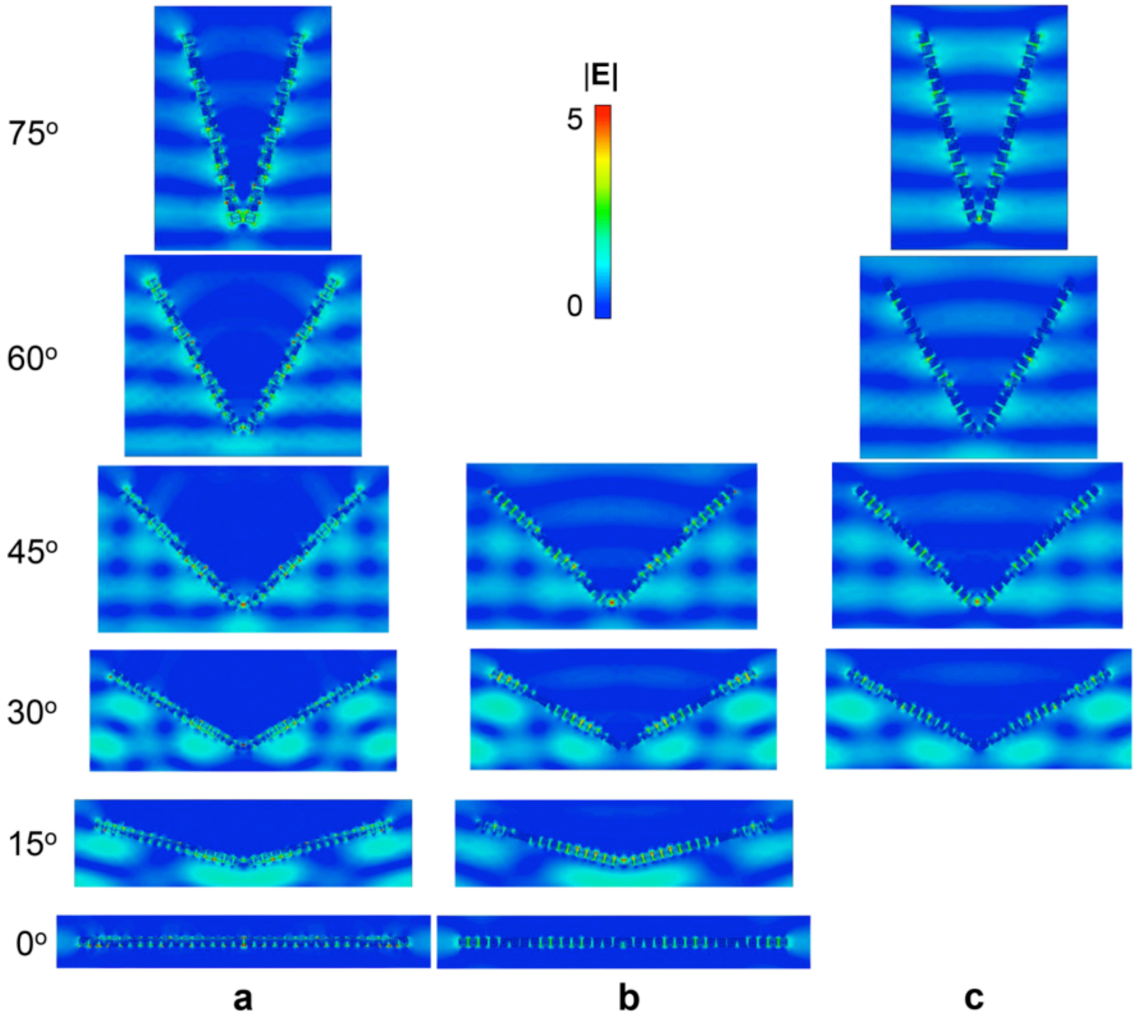

Figure S21: Normalized electric field distribution pattern along the cross-section of the nanoribbons with different folding angles. In each case, 'a', 'b', and 'c' correspond to the peaks shown in the extinction spectra of Figure S20 (iii). Incident light propagation and polarization directions are same as that in Figure S20 (i).

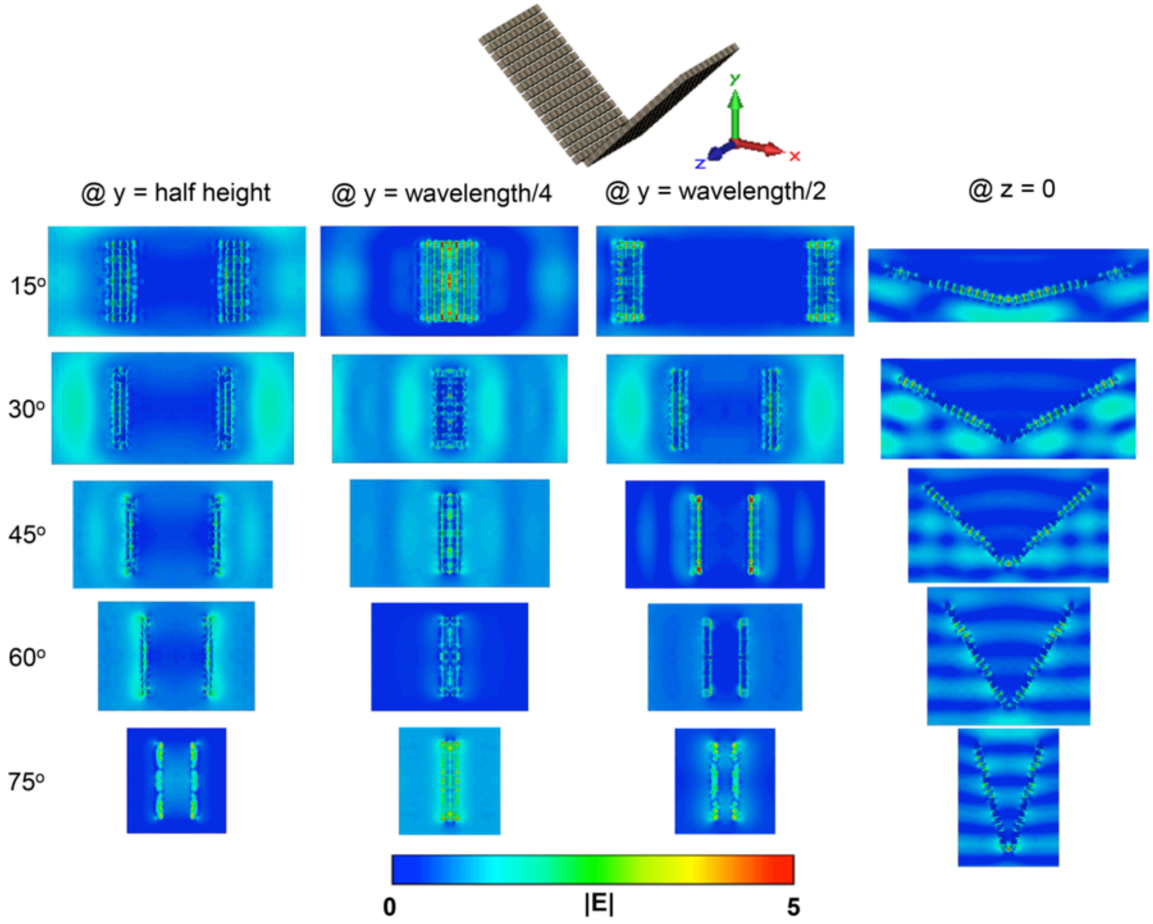

Figure S22: Normalized electric field distribution pattern along different *y*-planes (first three columns) and $z = 0$ cross-section of the nanoribbons with different folding angles. Incident light propagation and polarization directions are same as that in Figure S20 (i).

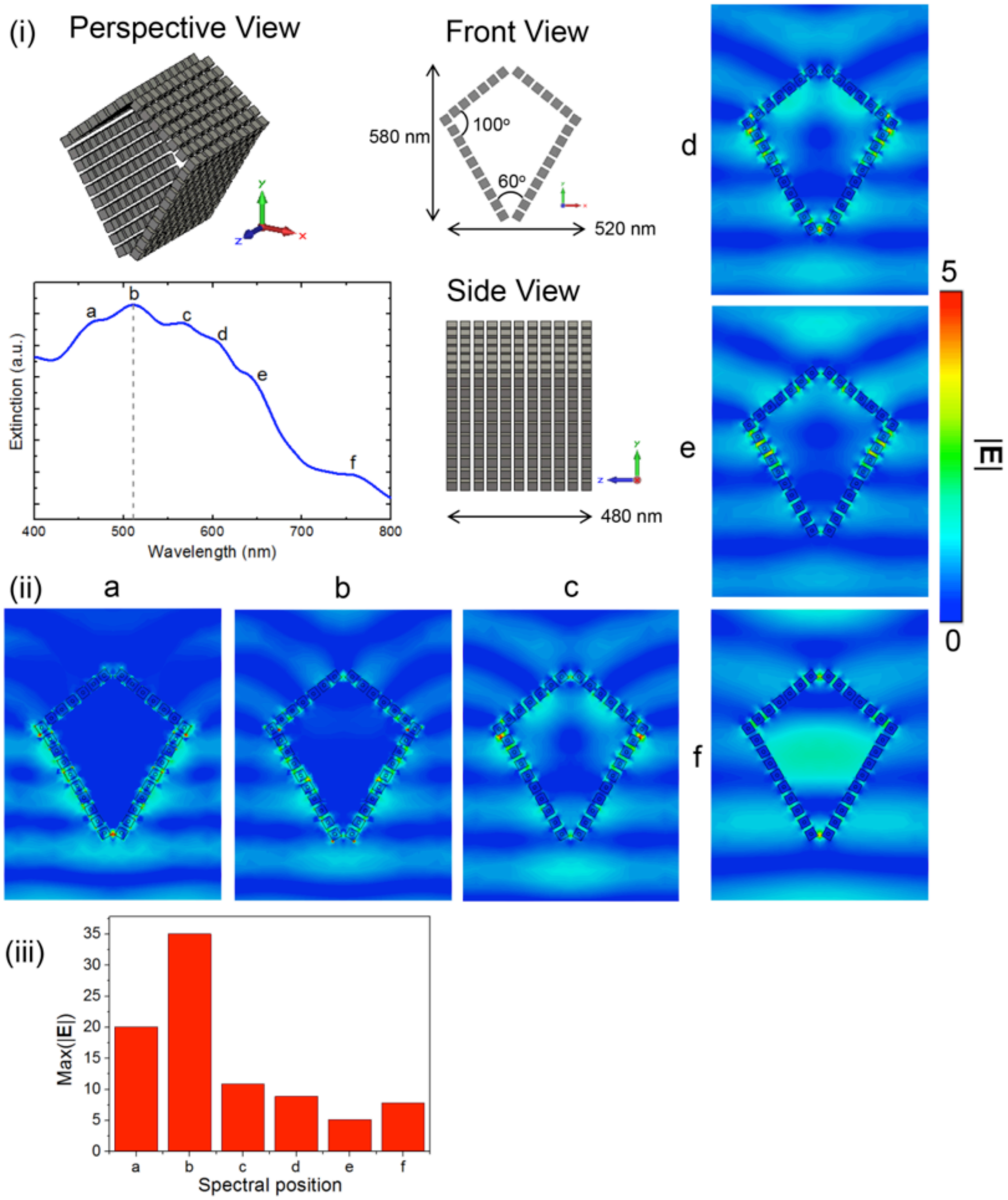

Figure S23: (i) Detailed schematic of the origami structure (shown in Figure 4d) and its optical response. (ii) Normalized electric field distribution pattern along the cross-section of the nanoribbons at different spectral positions marked in the extinction spectrum of (i). (iii) Maximum value of E-field (V/m) confinement in each case of (ii). Incident light propagation and polarization directions are same as that in Figure S20 (i).

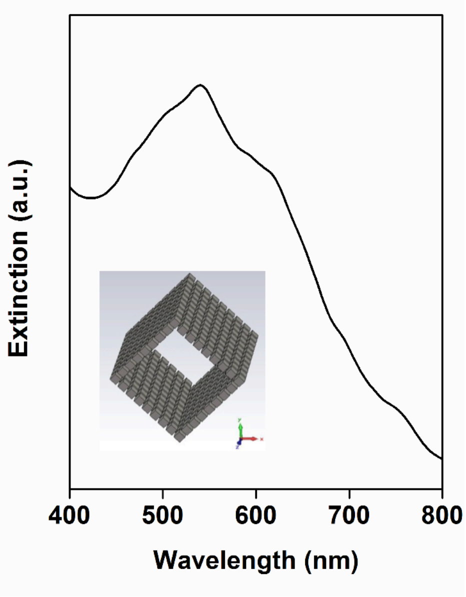

Figure S24. Model of a cube origami used for simulation. Incident light propagation and polarization directions are same as that in Figure S20 (i).

Section IV References

1. Jana, N. R.; Gearheart, L.; Murphy, C. J. Seed-Mediated Growth Approach for Shape-Controlled Synthesis of Spheroidal and Rod-like Gold Nanoparticles Using a Surfactant Template. *Adv. Mater.* **2001**, *13*, 1389-1393.
2. Nikoobakht, B.; El-Sayed, M. A. Preparation and Growth Mechanism of Gold Nanorods (NRs) Using Seed-Mediated Growth Method. *Chem. Mater.* **2003**, *15*, 1957-1962.
3. Ng, K. C.; Cheng, W. L. Fine-Tuning Longitudinal Plasmon Resonances of Nanorods by Thermal Reshaping in Aqueous Media. *Nanotechnology* **2012**, *23*, 105602.
4. Palik, E. D. *Handbook of Optical Constants of Solids;* Academic Press: New York, 1998.
5. Gong, J.; Zhou, F.; Li, Z.; Tang, Z. Synthesis of Au@Ag Core–Shell Nanocubes Containing Varying Shaped Cores and Their Localized Surface Plasmon Resonances. *Langmuir* **2012**, *28*, 8959-8964.
6. Bao, Q.; Tang, D. Y.; Loh, K. P. Broadband Graphene Polarizer. *Nat. Photonics* **2011**, *5*, 411-415.
7. Chang, J. R. F. a. C. L. Metal-Clad Fiber-Optic Cutoff Polarizer. *Opt. Lett.* **1986**, *11*, 386.
8. Eickhoff, W. In-Line Fiber-Optic Polariser. *Electron. Lett.* **1980**, *16*, 762-763.
9. Lee, C. C.; Proust, G.; Alici, G.; Spinks, G. M.; Cairney, J. M. Three-Dimensional Nanofabrication of Polystyrene by Focused Ion Beam. *J. Microsc.* **2012**, *248*, 129-139.